2005

QUANTIFICATION OF SURFACE DEFECTS USING PRIMARY HIGHLIGHT IN DIFFUSE ANGLE GRAY SCALE IMAGES

Subburengan Ganapathiraman
University of Kentucky, sgana2@uky.edu

ABSTRACT OF THESIS

QUANTIFICATION OF SURFACE DEFECTS USING PRIMARY HIGHLIGHT IN DIFFUSE ANGLE GRAY SCALE IMAGES

The thesis presented is an effort to gather all possible information of one particular type of common paint defect – the seed defect, from gray scale images of highly specular painted surface. The proposed approach in the thesis utilizes a white light source to illuminate the surface and utilizes a camera to capture its gray scale image at different diffused angles. While attempting to explain the physics of highlight formation in terms of location on the surface of a seed defect, the thesis also extends to utilize this information from gray scale images to accurately predict the parameters of seed defects including the height, size and position in real time. Since the primary highlight in a gray scale image is more defined, contrary to the past researches on diffuse angle images that use both primary / seed highlight and mirror highlight to estimate height of the seed, this thesis formulates a theory of highlight translation and estimates the height of seed based on primary / seed highlight. The other common type of surface defect - crater defect, is also addressed in the thesis.

KEYWORDS: Specular reflection, Highlight translation, Gray scale images, Diffuse angle reflection

Subburengan Ganapathiraman

December 12, 2005.

QUANTIFICATION OF SURFACE DEFECTS USING PRIMARY HIGHLIGHT IN DIFFUSE ANGLE GRAY SCALE IMAGES

By

Subburengan Ganapathiraman

Dr. Johné M. Parker
(Director of Thesis)

Dr. George Huang
(Director of Graduate Studies)

December 12, 2005

RULES FOR THE USE OF THESES

Unpublished theses submitted for the Master's degree and deposited in the University of Kentucky Library are as a rule open for inspection, but are to be used only with due regard to the rights of the authors. Bibliographical references may be noted, but quotations or summaries of parts may be published only with the permission of the author, and with the usual scholarly acknowledgments.

Extensive copping or publication of the thesis in whole or in part also requires the consent of the Dean of the Graduate school of the University of Kentucky.

A library that borrows this thesis for use by its patrons is expected to secure the signature of each user.

Name Date

THESIS

Subburengan Ganapathiraman

The Graduate School

University of Kentucky

2005

QUANTIFICATION OF SURFACE DEFECTS USING PRIMARY HIGHLIGHT IN DIFFUSE ANGLE GRAY SCALE IMAGES

THESIS

A thesis submitted in partial fulfillment of the requirements for the degree of Master of Science in Electrical Engineering at the University of Kentucky

By

Subburengan Ganapathiraman

Lexington, Kentucky

Director: Dr. Johné M. Parker, Associate Professor Mechanical Engineering, Lexington, Kentucky

2005

DEDICATION

To my Parents, Sister and Dhana

ACKNOWLEDGEMENT

Firstly, I would like to extend my sincere gratitude to my advisor Dr. Johné M. Parker for her untiring support, co-operation and guidance in this project. Words are short to describe her unbelievable energy level she brings to table during work and even afterwards. Her support and insightful advice were highly valuable during my period as a Graduate student.

I would also like to thank Dr.Jawahir and Dr.Khraisheh for agreeing to take part in my committee and provide their valuable insight.

This work would not have been possible without the support and suggestions from my lab mates Pradeep, Chen, Li, Yew Lim and Joe. I take this opportunity to thank each and every one of them.

I would also like to extend my sincere thanks to my friends who have in some way or other been helpful to my thesis.

Finally, the acknowledgement would not be complete if I don't mention my family for their love, support and encouragement. I thank every one of them.

TABLE OF CONTENTS

LIST OF TABLES

LIST OF FIGS

List of Files

SRThesis……1524 KB

CHAPTER ONE

INTRODUCTION

1.1 Motivation

Aesthetics of products is a critical component presented in the buying guide of today's customers. Also, surface appearance serves as a front-end tool in the eyes of a customer influencing the purchase of a product. Hence surface coating of consumer products is no longer done only to protect the surfaces from corrosive agents but also to serve as "bells and whistles" of the product. It becomes necessarily important for manufacturing industries to invest time and capital in an effort to make their products visually appealing. Examples of such industries include automobile, home appliances, office supplies, consumer electronics etc.

With current day manufacturers' emphasis on reduced *"lead time"* of products and "*zero defects"* through 100% quality inspection, it becomes essential to build a robust system that not only reduces the inspection time of painted bodies but also provides faster feedback to correct the process in order to prevent generation of waste and avoid rework. Present day industries either employ manual inspection of painted surfaces or an automated system primarily for identifying defects generated in the painting process. Although manual inspections have an edge over automated systems in places where quality metrics are difficult to set and requiring judgment to pass or fail, they are laborious, time consuming, inconsistent and provide very late feedback. Automated inspection systems eliminate the bottlenecks of manual inspection. However current systems are generally limited to specific applications and very well suit off-line. Most of them, while identifying the surface defects as just an

abnormality fail to provide information regarding shape and size and do not provide any kind of feedback on rectifying the process parameters and thereby hindering flow.

Hence the long-term objective is to design a system that incorporates an automated defect detection system with an additional feedback loop employed to provide valid information on the reasons for occurrence and possible parametric correction needed to avoid the recurrence of defects in future. Fig. 1 provides a comparison between the current system and the proposed system.

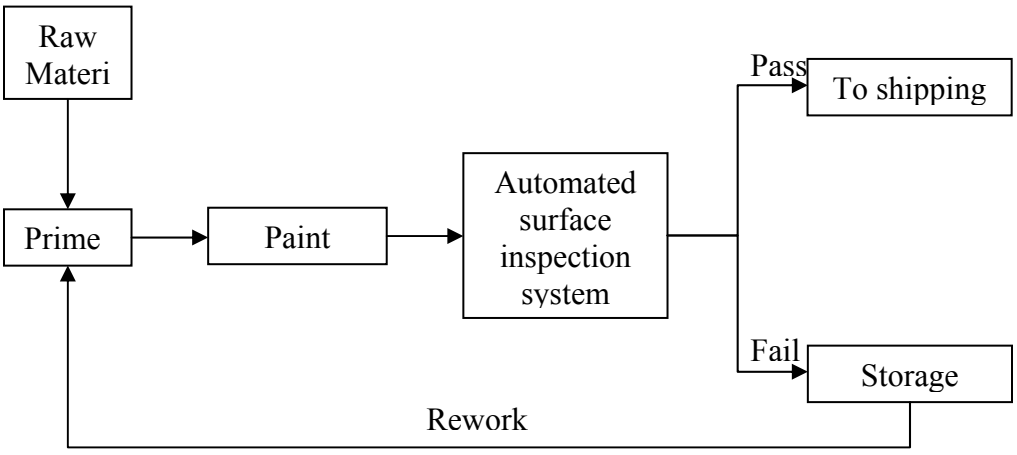

Fig.1a. Existing Automated Defect Detection System

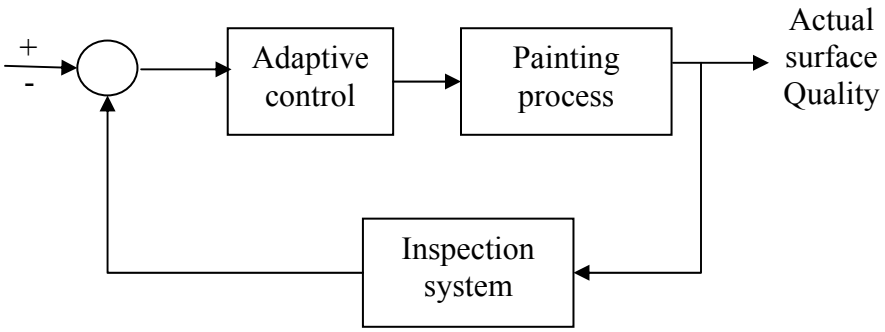

Fig.1b. Automated Defect Detection System with Feedback Control

Also current inspection systems utilize several optical sources for paint surface evaluation, which include laser, infrared light, diffused light etc. From a customer stand point, the source of light is a direct light source and hence the current research includes a direct light source for paint surface evaluation. The overall goal of the research project can hence be summarized in the following points:

- To develop a robust, online inspection system that guarantees faster feedback to prevent defect generation.
- To utilize white light source in order to understand the severity of defects like size and cluster that simulates the condition under which customers view a product.

The scope of the thesis is limited to device an inspection methodology that is faster, simpler and efficient that could fit in the overall Inspection System design.

1.2 Thesis Outline

The thesis is organized as follows: Chapter two presents the literature review of existing systems and related terminologies of underlying reflectance model over which the thesis is built; chapter three presents the experimental set up used for obtaining images; chapters four and five focus on preliminary set of experiments conducted, the theory of highlight formation and translation in seed defects and the procedure for obtaining seed height using the theory of highlight translation. Chapter six presents the preliminary investigation carried out on crater defects. Chapter seven provides the numeric results validating the theory of highlight translation. Chapter eight provides conclusions and future scope of the thesis.

CHAPTER TWO

LITERATURE REVIEW & TECHNICAL BACKGROUND

2.1 Current Inspection systems

Several commercial automated inspection systems are available in the market for identifying surface defects in painted surfaces. Some of them are discussed under this section with emphasis on principle of their operations and relative advantages and disadvantages.

An inspection method proposed by Wong Andrew et al [1] uses a convex shaped diffusing surface arranged relative to the light source to direct a gradient of light through the aperture in the form of a beam. The gradient in the reflective beam exposes any defects on the surface that are located on the beam and the location of the defects is noted. The gradient of the invention creates a shadow effect on the object. The shadow effect exposes the defect whether it is a dimple, a depression, a recoil, a roller mark, a projection or any other type of uneven surface. The shadow effect captured by the camera however poses difficulty during image segmentation because of a gradual intensity gradient in gray scale images.

Horigome et al [2] proposed the use of ultrasonic waves to detect defects. A pulse signal from an ultrasonic wave propagation medium is made to hit the object to be tested. The ultrasonic probe to obtain an echo signal receives a reflected wave of the ultrasonic wave incident on the object. The carrier frequency of the pulse signal is set so that the peak frequency of the echo signal becomes a predetermined frequency, and then the cycle count of the pulse signal is set so that the frequency bandwidth of the echo signal becomes a predetermined bandwidth. A defect present in the object is

detected in accordance with the echo signal output from the probe. The pattern of variation of echo signal does not give any useful information regarding the shape and nature of surface defects.

The high-speed flaw detection proposed by Smith et al [3] employs scattering of light as a mean to detect surface defects. The light detector and the light source are arranged relative to each other such that, in the absence of a surface flaw in the material, the light detector detects no light from the light source. The presence of a surface flaw in the material, results in light from at least one light source to be reflected off of the flaw and into the detector. Clear distinctions on the nature of the defect from the light scatter cannot be established using the system.

The two-mode surface defect system proposed by Lee Fredrick [4] comprises a first source of substantially collimated light, which passes along a first light path system to direct the collimated light to the test surface. The surface reflects the light, which is received and directed from the surface typically through at least some of the first light path system to an image processing apparatus. A second source of light is also provided, for providing substantially non-collimated light from the second source to a surface for testing in the holder, which may be the same surface for testing as above. This non-collimated light is reflected from the surface to image processing apparatus. The light may be non-polarized. By use of the two modes of testing, defects may be respectively detected at the outer surface of a transparent coating over an opaque surface, and defects in the opaque surface itself may also be detected.

Reynolds et al [5] used light to illuminate the test surface. The reflected light is then allowed to fall on a retro-reflective screen and on to the surface again and the re-

reflected light is then imaged to determine the presence of defects. One of the big advantages of these sorts of Diffracto-sight images relative to the normal highlight booth setup employing fluorescent light is that a large area of the part surface is covered without watching the edges of the fluorescent lights deviate due to variations in the curvature of the part. A good grade of retro reflective screen is required to achieve better results. The contrast of diffracto-sight images is better for smaller source dimensions.

Triangulation methods like projection techniques, laser-light techniques and shadow techniques and shape-from-shading techniques can be employed for diffusively reflecting surfaces. Reliability of such systems is lost when employed for highly specular paint surfaces. Stylus equipment and optical auto-focus scanners quantify surface defects to a high level of accuracy and precision. These methods are however too slow to be used in fast paced manufacturing environment. Rough industrial environments prevent the use of white light interferometry and Moiré methods because of their high sensitivity and high calibration cost [6].

3-D characterization of seed defects in specular surfaces proposed by Gnanaprakasam [7] uses a single image to quantify height of the defect using the seed and mirror highlight. This method estimates the real world distance between the primary and mirror highlight and derives the height of seed defect using mathematical geometry. The height of the seed estimated is a function of light source angle and camera angle. This method is accurate in predicting height of seed defect in absence of a paint pool at the base of defect or a seed whose image captured has distinct primary and mirror highlight. Presence of paint pool distorts the mirror highlight and hence affects the

predicted size of seed defect. This is illustrated by Figs 2.1a and 2.1b. Fig 2.1b indicates a larger seed with two distinct primary and mirror highlight. Fig 2.1a illustrates a smaller seed with mirror highlight and paint pool highlight merged together as a single highlight. Hence the application and accuracy of this model is limited to size of seed defects and painting technique.

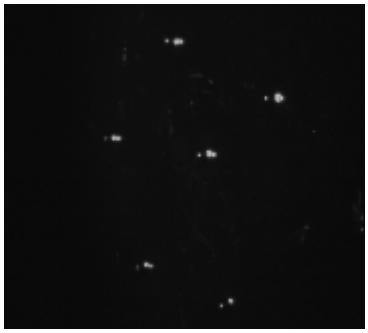

Fig. 2.1a Seeds with merged highlight

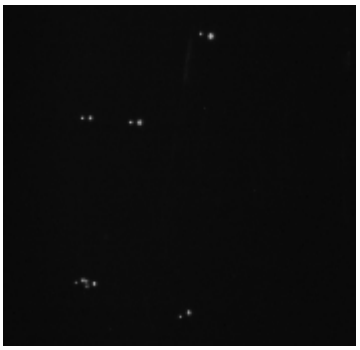

Fig. 2.1b Seeds with distinct highlight

2.2 Reflectance model

Reflectance models can be broadly classified as diffuse reflectance models and specular reflectance models. Past researchers have used Lambertian model for diffuse reflectance in shape-from-shading algorithms and for determining shapes of objects by photometric stereo. However they do not take into account the specular reflection off the surface [8]. On the other hand, the physical optics model proposed by Beckmann and Spizzicino and the geometrical optics model proposed by Torrence and Sparrow describe specular reflection mechanisms very well. The physical optics model, though it explains reflection from smooth and rough surfaces, has functional forms that are difficult to manipulate while geometrical optics model has a simpler functional form.

Nayar et al [9] presented a unified perspective of the above two models. According to this model, the total surface radiance is given as the sum of three components namely – radiance due to specular lobe, specular spike and diffuse lobe. The specular lobe and specular spike constitute surface reflectance and the diffuse lobe constitutes the body reflectance.

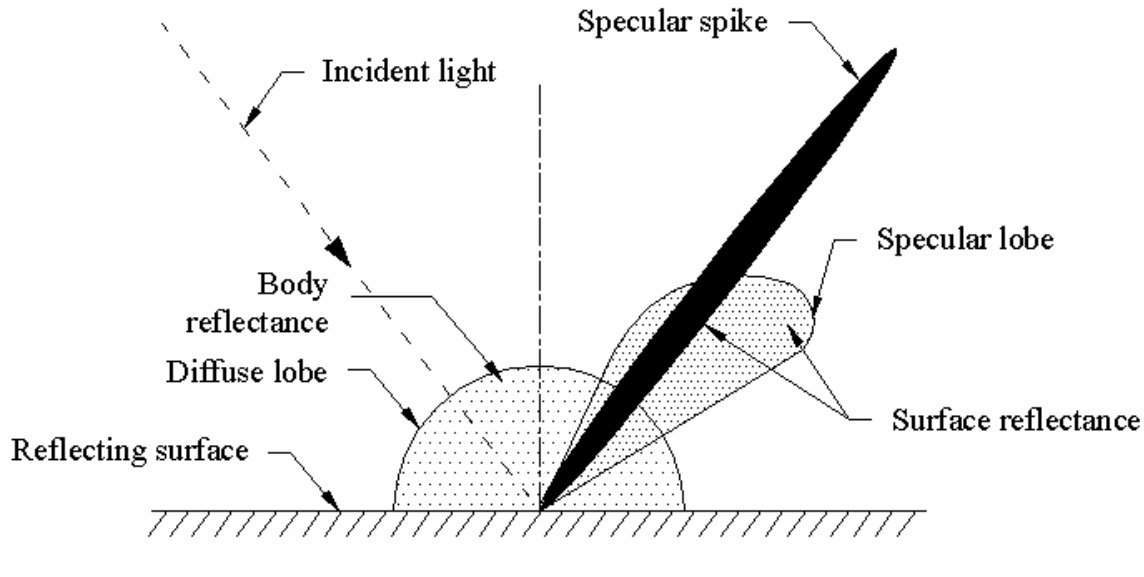

Fig. 2.2 Reflection off a surface and reflectance components

Thus the total radiance off the surface according to the model is given by the sum of radiance contributed by specular lobe, diffuse lobe and specular spike. The specular spike represents the mirror like property of the incident surface. Reduced surface roughness of the surface yields a dominant specular spike. As roughness of the surface increases the specular spike decreases and transforms to specular lobe. The specular lobe is due to the scattering phenomena of light off rough surfaces. The diffuse lobe on the other hand represents the internal scattering of light and is has a uniform distribution around the surface normal.

2.3 Camera model

The camera has been modeled as a gray-level sensor responsive to the energy/area impinging on the pixel [10]. (B. Horn, *Robot vision*. Cambridge, Mass.: MIT Press, 1986) The energy/area integral is approximated by:

$$E_{pixel} = \frac{\pi}{4}\cos^4\theta\left(\frac{d_p^2}{f^2}\right)L\tau \qquad \text{..... 2.1}$$

where,

L - Radiance impinging on the sensor pixel

τ - Exposure time

d_p - Effective lens diameter

f - Focal length

θ - Angle between sensor normal and ray impinging the sensor

Gray scale values of the image are obtained from the energy per area represented in eqn. 2.1 using:

$$G_{pixel} = K\left(\int_0^\infty E_{pixel}(\lambda)s(\lambda)d\lambda\right)^\gamma + G_0 \qquad \text{..... 2.2}$$

where,

G_{pixel} – Gray scale value of pixel

G_0 – Dark-current / zero illumination value

K – Sensor sensitivity

γ – System response linearity

The constants sensor sensitivity and system response linearity are determined empirically for a specific vision system.

CHAPTER THREE

SMALL SCALE EXPERIMENTAL SETUP

3.1 Construction

The schematic of the small-scale setup used for capturing the images is shown in Fig 3.1. The setup used for capturing the image mainly consists of the following components. They include:

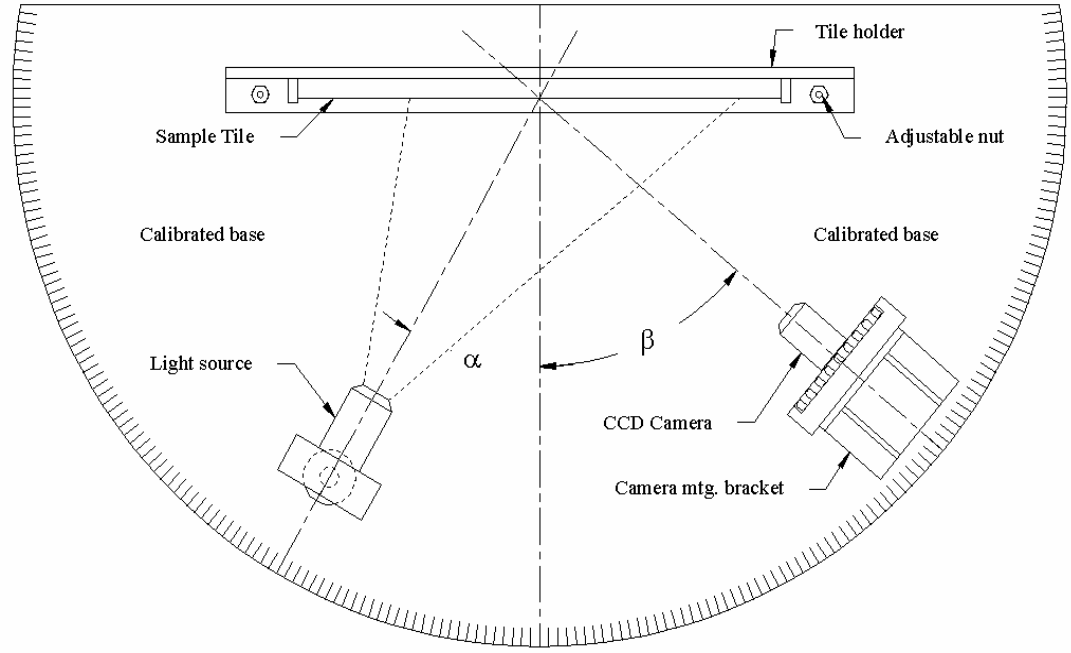

Fig. 3.1 Schematic of the small-scale setup used for imaging

1) A white light source:

The light source is mounted on the spectrometer base. The light source in the setup uses a 150 watt regulated white light conducted through an optical cable to minimize divergence of light. The wattage can be varied from 0 watts, representing dark current, to 150 watts for higher irradiance and illumination. It contains a collimator at

the end that renders the light rays parallel. The light intensity can be varied from 0 to maximum depending on the scene needed for image capturing.

2) DVT smart image sensor (Camera):

The camera used for capturing the image is a DVT smart image sensor with DVT LED lighting. The power requirement is 24V DC, 210mA (or minimum 5W supply). The image sensor has a resolution of 640 x 480 pixels with electronic shuttering of 10μs – 1 second exposure times. The shuttering can be varied in increments of 1μs. The camera is mounted on the spectrometer base by means of an L-shaped bracket.

3) Tile holder:

The tile holder is designed In-house and holds the sample to be imaged. It has three degrees of motion – along the X, Y and Z direction. The back and forth movement of the tile holder is made possible by means of a T-shaped sliding block that is guided in a T-slot. The sliding block can be locked at any desired location b means of grub screws provided. The height of the tile holder can be adjusted by means of adjusting screws provided on the ends of the tile holder. The horizontal or 'x' movement of the tile holder is achieved through stoppers on either side of the tile holder. All these three adjustments help to center the tile with reference to the camera center.

4) Calibrated base:

The light source, camera and the tile holder are mounted on a calibrated spectrometer base. The calibrated base in mounted on the floor using an adjustable tripod. The camera and light source can be individually moved over the circular base

making a maximum angle of 360°. This helps to fix the light source angle and camera angle for an image to be captured.

5) Defect sample:

The defect sample is created on a white ceramic tile base. The ceramic tile is usually painted black (in order to avoid the effect of color in initial studies) after placing a seed defect. The seed defects usually comprise mustard and coriander seeds or beads. These seeds are representatives of common types of defects that occur during the painting process which include unspecified bumps, inclusions, dust or dirt from atmosphere etc.

3.2 Initial adjustments in Setup

Before capturing an image or putting it into use, it is essential to perform initial adjustments and checks in the small-scale setup. The following points must be ensured before starting any experiment in the setup.

1) Leveling of base and sample tile holder – The spectrometer base and the tile holder have to be parallel to the ground. This is ensured by using a mercury spirit level and necessary adjustments are made to the base and holder using the adjustable nuts provided at the bottom of the unit. This adjustment corrects any ground unevenness present and prevents it from getting transferred on to the image.

2) Creating a reference tile – It is a good practice to know the center of light source and center of the camera. In order to determine this, a sample tile of the same dimension as the imaging tile is marked with a vertical and horizontal cross lines passing through the center of the tile. This tile is used as a reference for fixing the centers of light source and camera.

3) Setting the Camera – The sample tile shown in Fig. 3.2 (with or without the circle) is placed on the tile holder. The DVT sensor is moved to angle 0°, i.e. perpendicular to the tile and the camera is switched on. The image of the sample tile can now be viewed on the computer screen. Now a horizontal line and a vertical line are drawn on the image shown on the screen at pixel locations 240 and 320 respectively. The intersection of these two lines represents the camera center.

The objective of initial camera setup is to align the vertical and horizontal lines drawn on the tile and the image and make them coincide at all angles as the camera is moved from this angular position to as large as 75°. The horizontal shift and the vertical shift of the cross lines can be corrected by moving the tile placed on the tile holder. Any angular shift between the cross lines in the image and tile is adjusted by tilting the camera (as the tile is already parallel to the ground because of Step 1).

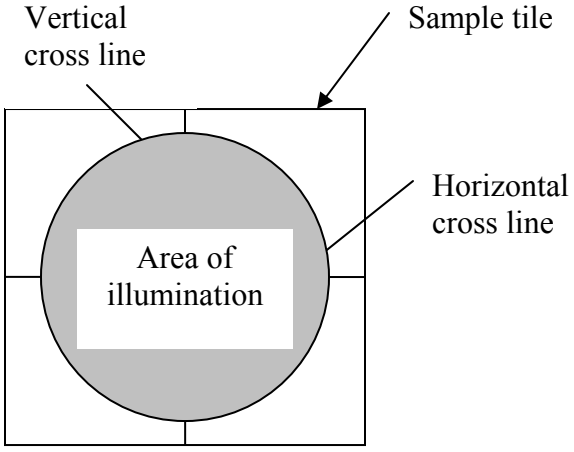

Fig. 3.2 Sample tile for Initial Adjustments and settings

Once all these adjustments are made at 0°, the camera is moved along the calibrated base to various angles. It can be noted that the vertical cross lines of image and tile separates out as the camera is moved. This shift is corrected by moving the tile holder

back and forth as required, till no separation of vertical cross lines is observed. This ensures that the camera center does not vary with varying angular positions. Also the tile position in the holder is fixed by means of a reference stopper. This serves as a reference for positioning a tile to capture image at any angle in future.

4) Positioning the Light source – The light source is positioned at 0° and the light source is made to strike a clear sample tile. The maximum diameter of the illuminated area of light (due to divergence) is measured by means of a vernier caliper. This circle is superimposed on the sample tile (tile with cross lines) as shown in fig. 3.2.

This tile is now placed in the tile holder. The illuminated area may not be exactly coinciding with the circle drawn on the tile. The light source is adjusted to move up or down or tilted to make the boundary of diverged light source coincide with the circle drawn on the tile. Once adjusted, the adjusting nuts are tightened to ensure that the position of light source does not change any further.

Once all these adjustments are made, the positions of light source, camera and the tile holder are locked and ensured that they do not change during experimentation and imaging. The following check points need to be ensured before capturing the image:

1) The position of tile holder and the tile need to be ensured in reference position set. If not adjust to set it at reference position.

2) Ensure light illumination is within the circle of reference tile when light source is square to the surface of the tile. Illumination outside the circle indicates that the light source is not perpendicular to the tile and the angle of light source set using the calibrated base may not be correct anymore.

3) Move the camera along the calibrated base and ensure the center of the camera and center of the tile are aligned.

3.3 Capturing Images using small scale setup

Once the initial setups are carried out, the tile whose image is to be captured is placed on the tile holder. The camera and light source are switched on. The intensity of the light source can be adjusted to achieve the necessary contrast in the image. The light source and the camera are moved along the calibrated base to any angle required by the experiment.

The camera when turned on displays the image on screen. Before capturing the image, it needs to be ensured that the imaging pixels do not bleed. Bleeding is the process by which the excess energy impinging on a sensor element is dissipated to adjacent pixels. Bleeding occurs when an image sensor is over exposed to light due to excessive light intensity or excessive exposure time. One or more of the following may be done till bleeding disappears.

- Reduce the intensity of white light source
- Turn on the anti-blooming option in the camera (used as a last resort since the linearity of the camera model is affected)
- Reduce the exposure time of electronic shuttering

Once the image on the screen is clearly visible without bleeding, the image may be captured. The image can then be stored in the computer or on the camera.

The parameters of the experimental setup like the angle of divergence of light source and the maximum area of illumination wherein the defects are to be positioned in order to capture images can be found in Appendix A.

3.4 Images from diffuse angles

Experiments were carried out in order to understand the specular reflection of light due to spherical seed defects from diffuse angle. The area of diffuse angle is specified in fig. 3.3. The areas highlighted as *"Area 1, Area 2 and Area 3"* defines the region of diffused angles for a light ray incident over a highly specular surface at an angle of *'i'*.

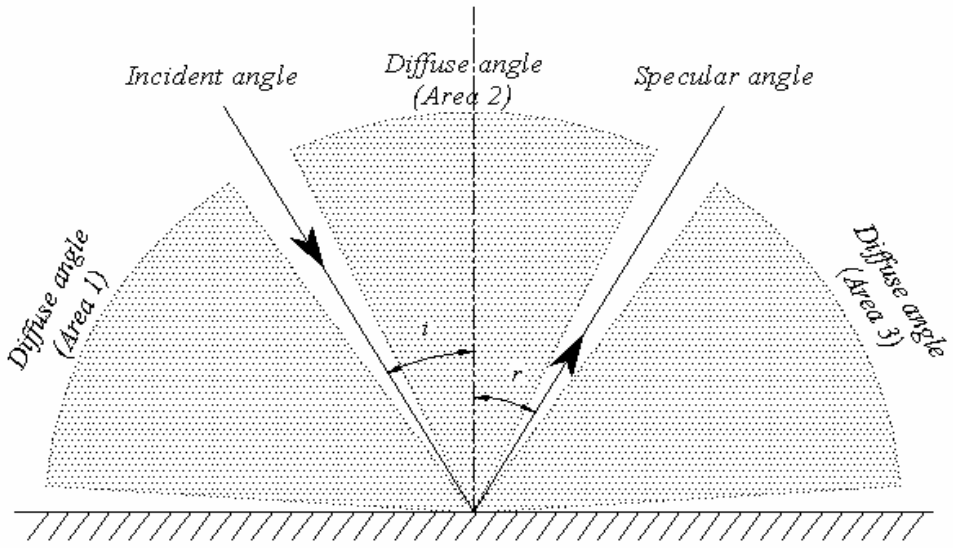

Fig. 3.3 Area of diffused angles over a highly specular surface

The region utilized for studying the seed highlight is restricted to area 3 in the fig. 3.3 due to constraints in the experimental setup and also due to the fact that highly contrast images with distinct primary and secondary highlight could be observed b placing the camera in Area 3 [7].

CHAPTER FOUR

THEORY OF HIGHLIGHT FORMATION

4.1 Theory behind the images obtained from specular and diffused angle:

According to law of reflection described under section 2.2, light gets reflected off a surface at the same angle of incidence with reference to the normal at that plane. This is true for both planar and non-planar surfaces. In case of planar surfaces, the surface normals are parallel to each other and hence the angle of reflection with reference to horizontal remains the same. These kinds of surfaces can hence be termed as specular surfaces because the resultant rays of reflected light travel primarily in one direction. The resultant reflection is called *specular reflection* of light, which is characterized by a sharp beam of light

In case of non-planar surface or in general a surface with irregularity, the angle of reflection when measured with reference to the horizontal keeps changing for the same angle of incident light. This is due to the fact that the localized normal at any point keeps changing (not parallel to each other as in previous case). This causes the reflected rays to travel in different directions resulting in *diffuse reflection* of light.

Based on above cases, it can be deduced that specular reflection and diffuse reflection of light are outcomes of light getting reflected off a surface, the nature being dependent on the topography of the surface under consideration. In short, a uniform surface produces scattering in a precise direction whereas an irregular surface produces a random scatter.

Consider a plane surface illuminated by a collimated source of light as shown in fig. 4.1. The bundle of light rays striking the surface gets reflected off the surface

following law of reflection. Each ray in the bundle is subjected to the law. The resultant image when viewed by the camera traces the source of light. On the image plane, a compact illuminated area is formed when viewed at the same angle as incidence with respect to the normal to the surface under consideration.

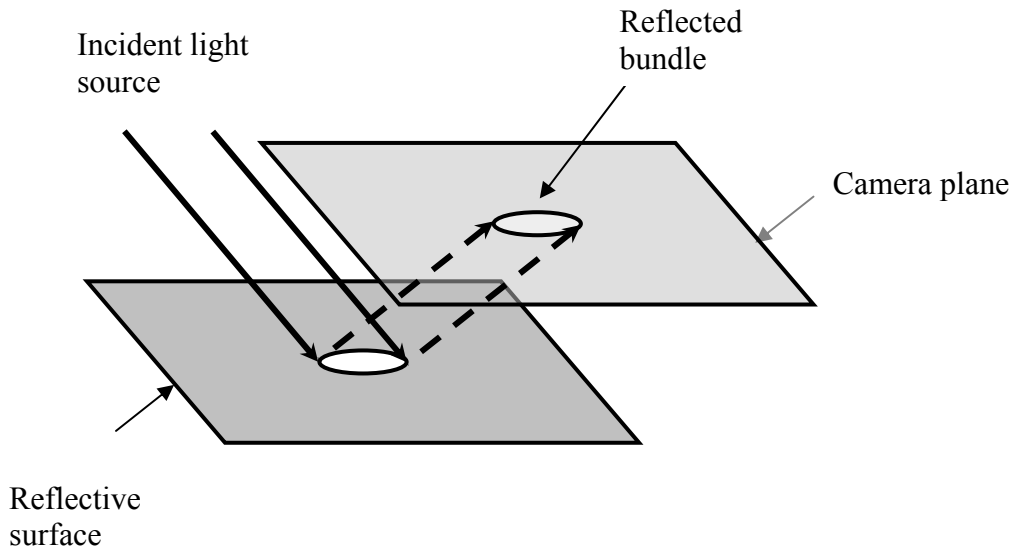

Fig. 4.1 Reflection of ray bundle at specular angle

The image obtained in the camera plane is due to the illumination of the pixels by the reflected light rays from the plane surface. The image obtained is exactly the replica of the light source as all of the light rays get reflected back towards the camera in specular direction. This kind of image is obtained only when the camera is at the same angle as the light source with respect to the normal. Moving away from the specular angle into the diffused region described in section 3.4 results in lesser and lesser reflected rays to travel in camera direction till there is no significant reflected ray going in that direction. Fig. 4.2a and 4.2b indicate images taken at 30˚ (specular angle) and 70˚ (Off-specular / Diffuse angle) respectively. As expected, the image at 70˚ does not reveal any sign of reflected rays at all.

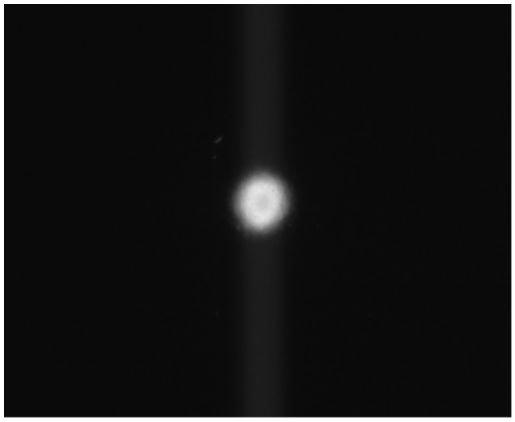

Fig. 4.2a Image at specular angle *Fig. 4.2b Image at off specular/diffuse angle*

In case of a highly irregular surface, the illumination in the camera plane is uniform as no single bunch of reflected rays are given out by the surface.

4.2 Phenomenon of highlight formation in near spherical seed defects

The following section is an attempt to explain the phenomenon of highlight formation, using a two dimensional analytical approach, over a spherical seed defect in a specular painted surface.

Let a seed of very small radius compared to the area of illumination be placed over the painted surface. The seed is positioned in such a way that the central light ray strikes the center of the seed. The incident light source makes an angle of 30˚ with the vertical. Now the image of this seed is captured at two different diffuse angles, 50˚ and 70˚. The images obtained at these two angles are presented in Figs 9a and 9b respectively. As discussed section 4.1, the reflection off the plane surface is obtained at 50˚ (fig. 4.3a) as this is very close to the specular angle and an absence of light source can be noted for the 70˚ angle in fig. 4.3b. Apart from these light rays

recorded, a distinct near spherical highlight can be seen because of off-specular reflection of light from the seed surface.

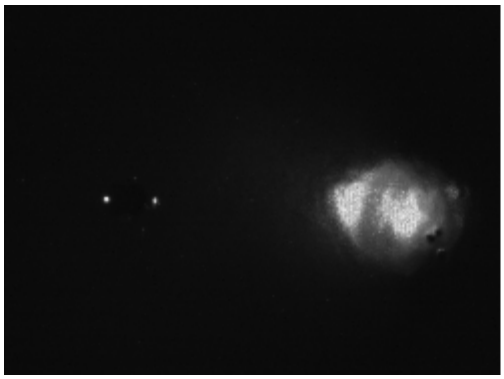

Fig. 4.3a Image of seed at50˚

Fig. 4.3b Image of seed at 70˚

Since the seeds are too small compared to the illuminated area it may be assumed that all the rays striking the seed are at the same angle with vertical. The whole surface other than the region of the seed sends back the light to the camera at the same angle with respect to the normal at which the light ray strikes the surface. This is not true in the region where the seed is positioned. The normal on the surface of the seed changes with position. Hence the incident angle measured with respect to the normal also changes. This results in different reflected angles with reference to the vertical even though the angles of incidence and reflection is same at a particular point over the surface of the sphere.

For the sake of simplicity, consider a slice of disc of infinitesimally small thickness *'δx'* cut at the center of the sphere by introducing two planes very close to each other. Now this disc can be treated as the circle with diameter *'d'* which is the diameter of the seed placed over the surface. A light source is allowed to illuminate this circle or rather a disc with very small thickness. A part or portion of this circle is responsible

for reflecting the light towards the camera. A definite sector angle, as shown in fig. 4.4, with center same as the seed center can be accounted for defining this area on the surface of the disc.

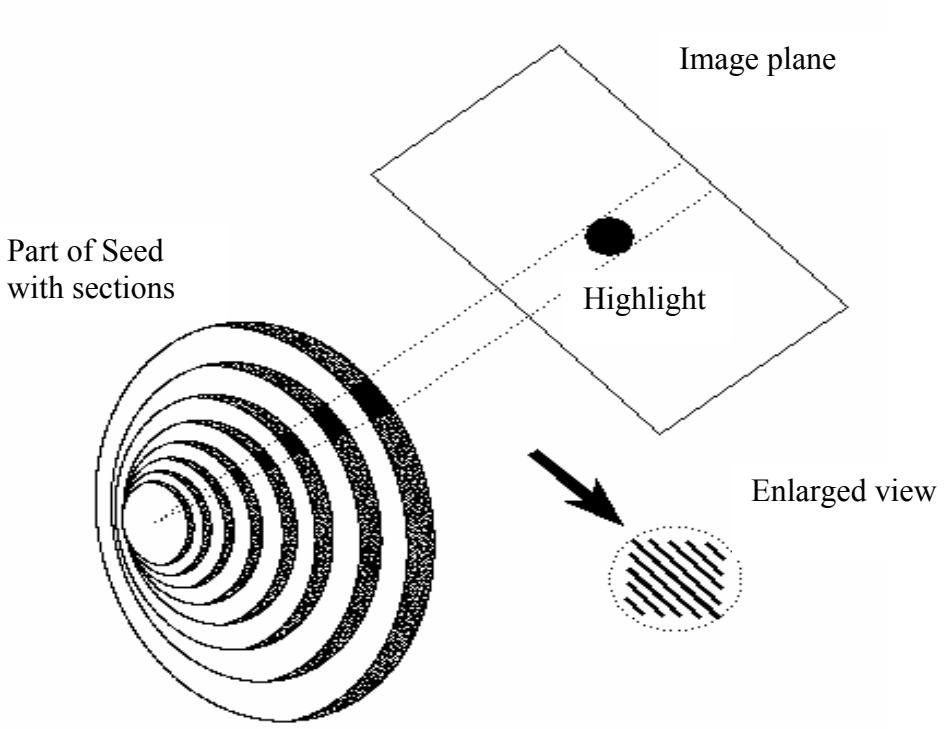

Fig. 4.4 Formation of circular highlight

The highlight area can be treated as a part of the disc with the same thickness as the disc. In this particular case this can be treated as an arc that is responsible for forming this highlight.

Now consider another disc of same thickness *'δx'* and diameter *'d-Δd'*, where *'Δd'* is infinitesimally small. The center of this disc is concentric with the center of the previous disc considered. The light is then allowed to illuminate this circle and subsequently another highlight arc is obtained in the camera plane. The reflected rays are made to strike the imaging plane. It is to be noted that the area enclosed in the

same sector angle constitutes the specular reflection. The only difference between this arc and the previous is the reduced length. This reduction in length of arc of highlight is because of the reduction in diameter by *'Δd'*.

Consider similar discs each time with a reduced diameter than the previous. The size of the highlight arc decreases every time till it becomes feeble and vanishes away because of the insufficient sector area along the circumference of the circle. Now stacking all these circles in the descending order of the diameter on either side of the largest circle with diameter *'d'* yields a sphere and the stack of arcs constituting the highlight forms a circle. The sphere corresponds to the seed and the circle corresponds to the highlight formed on the surface of the seed. This explains the formation of a circular highlight for a spherical defect placed on the surface of the tile.

4.3 Location of the highlight spot on the surface of the seed

The following section aims to provide an approximation for the position of the highlight formed over the surface of a seed. The highlight captured by the camera is due to the specular reflection of seed in the direction of the camera [7]. In order to understand the position of highlight, it is essential to study the reflection / scattering of light from the surface of the spherical seed.

Consider a seed placed over the top of a perfectly flat, highly reflective surface. Let *'α'* be the angle of incidence of light with the vertical. Since the seed is small when compared to the illuminated area, it may be assumed that all the light rays strike the surface of the seed with incident angle *'α'*. The reflection from the surface of the seed

depends on the local normal at that point, which passes through the center of the seed. As such the normal of the seed keeps changing at each and every point on the surface of the seed. Fig. 4.5 illustrates the seed position, angle of incidence of light source and the camera position at diffuse angle. The thick lines represent the incident light rays, the dotted line indicates the normal at that point and the broken lines indicate the path of reflected rays from the point of incidence.

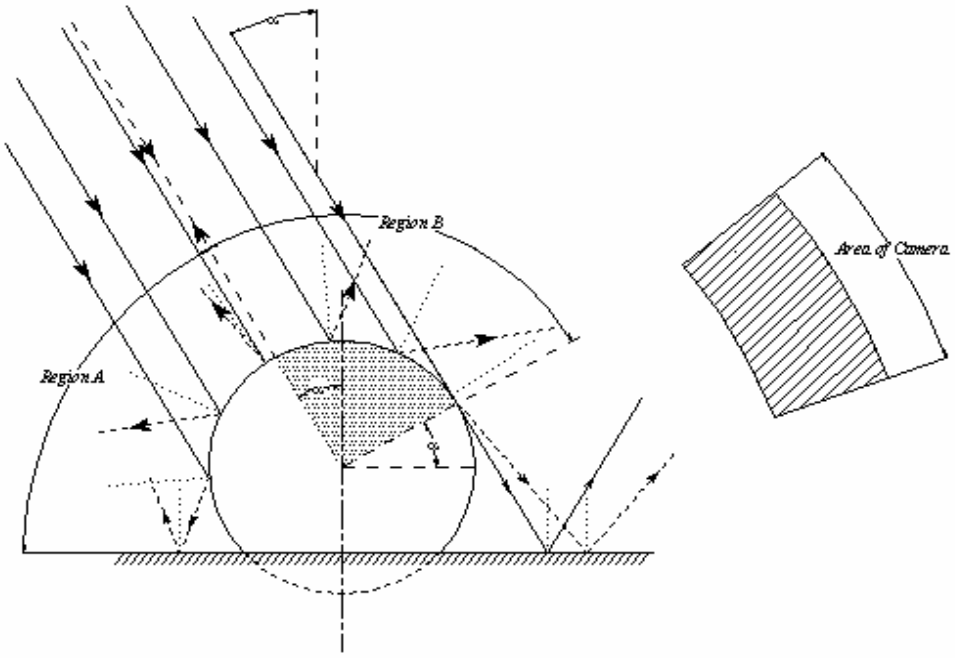

Fig. 4.5 Reflections over the surface of a spherical seed

From the Fig, two distinct regions *'Region A & Region B'* can be isolated. Consider the region *'A'* of the seed that lies to the left of the point at which the light ray at incident angle meets the seed center when extrapolated. The normal at this point lies exactly overlapping the incident ray. Hence the ray is retro-reflected towards the direction of light source. Any light ray that strikes to the left of this ray has its reflected ray turning away from the direction of the camera. Hence this region *'A'*

may very well be eliminated, as it is not responsible to form the highlight captured by the camera.

Consider the region *'B'* right to this incident ray. The reflected rays from the points at least travel in the direction of the camera though the camera may not capture it. The region *'B'* starts at an angle *'-α'* with vertical and extends to the maximum point where incident ray is tangential to the seed surface. This maximum point also characterizes the first light ray that strikes the plane surface by just escaping the seed and gets reflected in the specular direction of the plane surface. Any point beyond this tangent to the right of the seed is not under the direct illumination of the light source and hence cannot account for the specular highlight formed on the top of the seed.

Based on above discussion it can be observed that the region that is responsible for forming the highlight is included within a sector of 90˚ angle. This region is bounded by angles α and $(90+\alpha)$, the angles being measured with respect to horizontal.

This region of interest can now be divided into as many elements as possible by a definite number of points. At each of these points, the incident ray strikes the sphere at an angle equal to α with respect to the vertical. Fig. 4.6 indicates the reflection off a point '*P*' in the region of interest.

Let *'P'* be any point on the region of interest and let φ be the angle of this point with the horizontal. The normal at this point also makes an angle φ to the horizontal at this point (line from center). Hence,

Angle of the normal at 'P' with the vertical $= 90 - \varphi$

Angle of incident ray with the normal $= 90 + \alpha - \varphi$

Hence the reflected ray in the same plane as normal also makes the same angle with the normal, by the law of reflection. Therefore,

Angle of reflected ray with the horizontal = $\gamma = 2\varphi - (90 + \alpha)$ ….. 4.1

Hence any ray in the region of interest to the right of the vertical makes an angle of 'γ' with the horizontal.

The reflected rays from all these points can be made to hit the viewing plane to determine the cluster of rays hitting a particular region in the viewing plane. The center of this cluster of rays can then be treated as the center of the highlight.

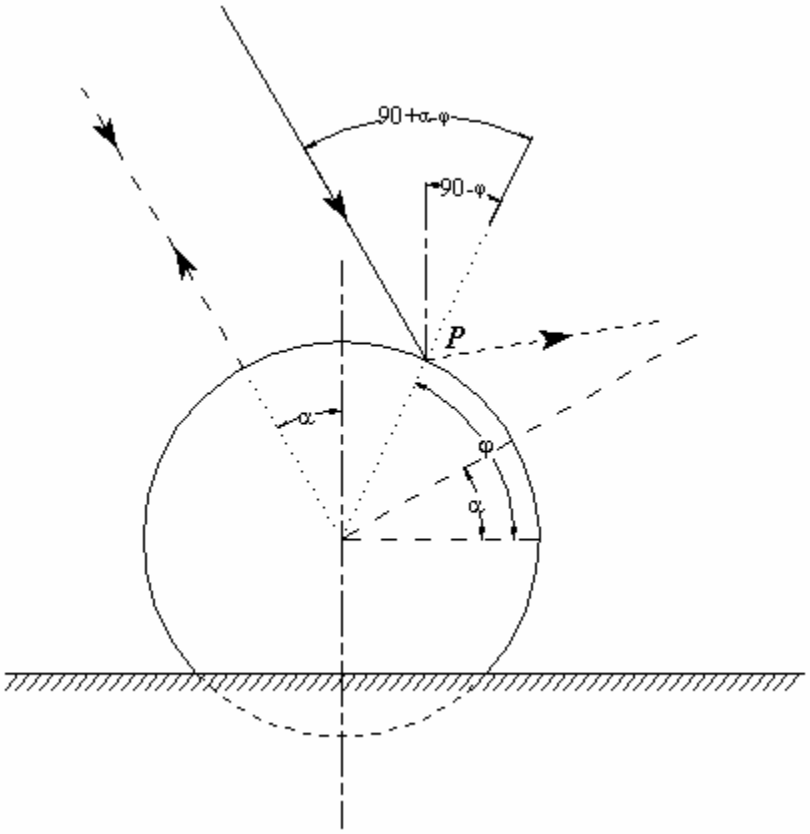

Fig. 4.6 Indicating Reflection off a point in area of interest

Let *'r'* be the radius of the seed. The point *'P'* on the surface of the seed in 2-D, then has a polar co-ordinate of:

$$x_1 = r\cos\varphi \quad \& \quad y_1 = r\sin\varphi \qquad \text{.....4.2}$$

The angle of the reflected ray at this point can be obtained from eqn. 4.1.

$$\gamma = 2\varphi - (90 + \alpha)$$

The slope of the reflected ray is then given by:

$$m = \tan\gamma$$

The general equation of the reflected ray in slope-intercept form can be given as:

$$y = mx + c$$

where *'c'* is the y-intercept and *'m'* is slope of the line

Hence in order to find the y-intercept of the reflected ray, replace *'x'* and *'y'* by the co-ordinates and m by the slope of the line.

$$y_1 = x_1 \tan\gamma + c$$

From eqns. 10,

$$r\sin\varphi = r\cos\varphi\tan\gamma + c$$

Therefore,

$$c = r[\sin\varphi - \cos\varphi\tan\gamma]$$

Hence the equation of the reflected ray is given by:

$$y = x\tan\gamma + r[\sin\varphi - \cos\varphi\tan\gamma] \qquad \text{.....4.3}$$

Let *'β'* be the angle of the camera with the vertical. The viewing plane hence makes an angle of *'β'* with the horizontal measured clockwise. Let *'z'* be the

perpendicular distance between the viewing plane and the seed center. The y co-ordinate of the viewing plane at the horizontal is 0 and the x co-ordinate is given by:

$$x_2 = \frac{z}{\sin\beta}$$

Hence the co-ordinate at the point where the viewing plane meets the horizontal axis of the seed is given by (z/sinβ, 0). The slope of the viewing plane is given by:

$$m = \tan(180 - \beta)$$

Following the same procedure as eqn. 11 is obtained, for the viewing plane we have:

$$c = \frac{-z\tan(180 - \beta)}{\sin\beta}$$

Hence the equation of the viewing plane is given by:

$$y = x\tan(180 - \beta) - \frac{z\tan(180 - \beta)}{\sin\beta} \qquad \text{…..4.4}$$

Solving equations 4.3 and 4.4 gives the co-ordinates on the viewing plane where the reflected ray strikes.

Now many points $P_1, P_2, P_3 \ldots , P_n$ can be taken in the region of interest and the co-ordinates of the reflected ray and viewing plane intersection is found. The above procedure was simulated using MATLAB. It was observed that in a certain region there exists a cluster of points due to reflected light and this reflected light scarce out on either side of this cluster. This cluster can then be treated as the bunch of rays that strike the viewing plane to form the highlight arc (section 4.2). The center of the arc can then be treated as the center of the highlight formed.

The mid point of this cluster was then traced back to the seed surface to locate the point on the seed that reflects the light ray to the centroid of reflected rays cluster. It

was noted that the point on the seed surface corresponds to the angle of bisection of the light angle and camera angle passing through the center of the seed. This is expected to occur for any perfectly specular surface that holds a seed defect.

CHAPTER FIVE

EXPERIMENTS ON HIGHLIGHT TRANSLATION & SEED DEFECT QUANTIFICATION

5.1 Correction factor for seed height

The initial assumption that assumes the highlight on top of the seed in Gnanaprakasam's hypothesis [7], needs correction based on the discussion in section 4.3. It is found that the highlight forms at the bisection of light source angle and camera angle. A correction factor for the height (estimated using mirror reflection from single gray-scale image) is proposed in this section. Fig 5.1 indicates the location of the highlight and seed geometry used for estimating the height ratio. In the following discussion for correction factor and seed height estimation, the seeds are assumed to perfectly spherical and are place on a highly reflective specular surface.

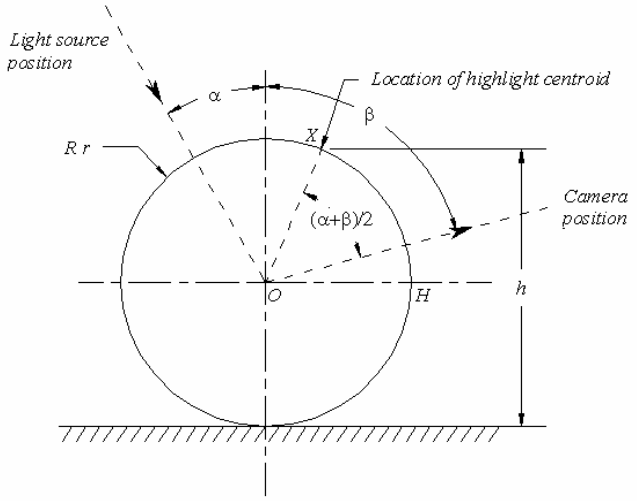

Fig. 5.1 Location of highlight over a spherical seed

Let '*r*' be the radius of the seed placed over a highly specular surface. The angle of incidence and camera angle are *'α'* and *'β'* respectively. Let '*h*' be the height of the

highlight from the specular surface. From the discussion under section 4.3, the highlight is formed at the bisection of camera angle and light source angle as indicated by point '*X*' in fig. 5.1. From the Fig,

$$\angle XOH = (90+\alpha) - \frac{\alpha+\beta}{2} = 90 + \frac{\alpha-\beta}{2}$$

$$h = r + r\sin\left[(90+\alpha) - \frac{\alpha+\beta}{2}\right] \Rightarrow h = r\left[1+\cos\frac{\alpha-\beta}{2}\right] \qquad \ldots\ldots 5.1$$

Hence the ratio of height of highlight to height of seed is given by:

$$\chi = \frac{h}{2r} = \frac{1}{2}\left[1+\cos\frac{\alpha-\beta}{2}\right]$$

Impact of correction factor 'χ' for differences in light and camera angle:

The influence of correction factor plays a major role in accurate determination of seed height depending on the light source angle and camera angle.

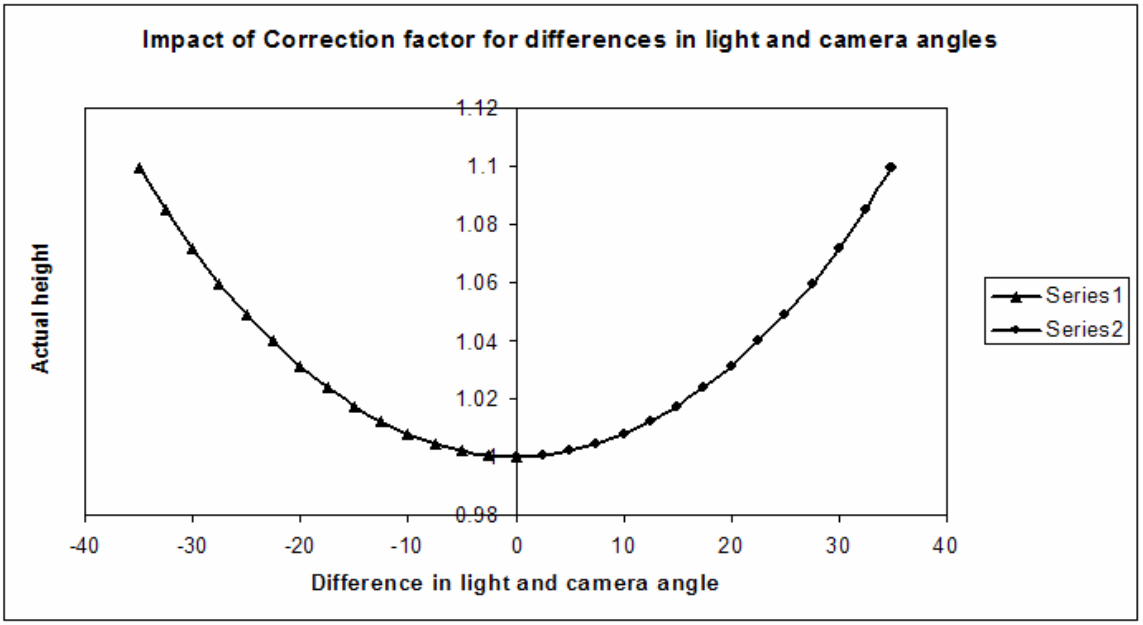

Fig. 5.2 Variation of seed height with difference in camera and light angles

With a fixed light source angle, when the camera angle is increased, more error is observed in height estimation when the initial assumption (seed highlight forming at the top) was used. However moving the light source to a wider angle may counteract this. This phenomenon is illustrated in fig. 5.2.

The values of *(α-β)/2* are plotted along the X-axis. For these differences in light and camera angle and for a constant initial seed height (highlight height from the stratum), say 1, the actual height is estimated. It can be seen that when the difference in light and camera angle is zero, the initial height obtained equals the estimated actual height of the seed, i.e. the highlight forms at the top of the seed when the camera and light source angles are equal (line along the center becomes the bisection angle of α and β). In other regions, the influence of correction factor can be seen. Similarly the impact is large with larger differences in light and camera angle.

5.2 Highlight translation on a 2-D plane:

From discussions in section 4.3, the highlight is formed at the surface of the seed at the bisection of light source angle and camera angle. It can be deduced from the argument that upon changing the light source angle or camera angle or both, the position where the highlight is formed can be varied. For all the experiments conducted, the light source angle is fixed as *'α'*. The variation in position of the highlight can then be achieved by changing the view angle of the camera, i.e. for a light angle of *'α'* and any camera angle *'β_i'*, the angle of highlight with respect to horizontal (from section 5.1) is given by:

$$\angle XOH = (90 + \alpha) - \frac{\alpha + \beta_i}{2} = 90 + \frac{\alpha - \beta_i}{2}$$

The substrate or the tile surface represents the XY plane. Any seed positioned on this plane has a height associated with it. The height of this seed actually lies along the *'Z'* axis perpendicular to this plane. Consider the fig. 5.3 where the seed is positioned on the XY plane. Light strikes the seed at angle *'α'* and the camera angle is *'β'*. Light gets scattered off the seed and highlight is formed on the surface at point 'X' as shown in fig. 5.3.

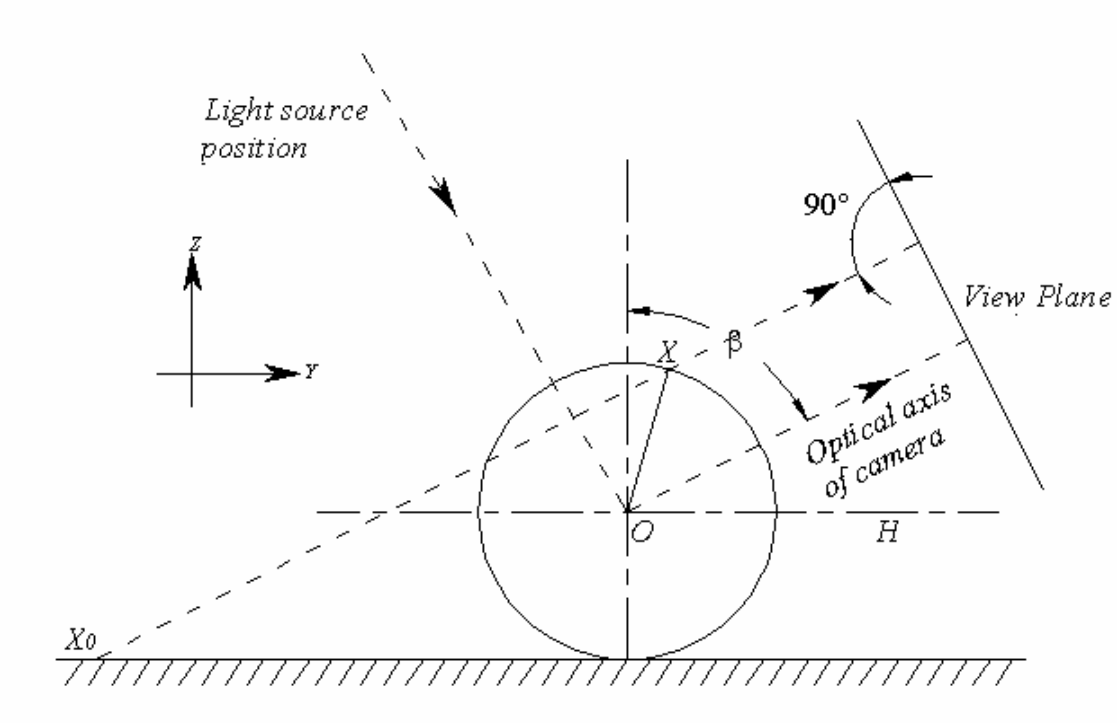

Fig. 5.3 Highlight position as seen by the camera

This highlight is viewed by the camera positioned in 3-D space. The image of the highlight captured by the camera appears as a circular bright spot in the two dimensional plane, i.e. the camera views the object as it is placed in the XY plane.

When the camera views the centroid of the highlight, it actually is viewed as a point located on the XY plane. This is due to the fact that the Tsai's calibration technique

assumes a coplanar real world scene [7]. Since the light traveling towards the camera moves along a straight line and the image plane is considered perpendicular to the camera axis, the location of the highlight on the XY plane can be obtained by drawing a line perpendicular to the view plane passing through the highlight spot and intersecting the XY plane. Thus the camera views the point *'X_o'* for a highlight formed at point *'X'* as shown in fig. 14.

Based on this discussion above, it may be noted that by changing the angle of camera 'β', the highlight shifts to a new position other than *'X'* over the sphere and this leads to translation of point *'Xo'* to a new position along XY plane in the direction of 'Y-axis'. The wider the change in angle *'β'* between two positions of camera, the bigger the translation of highlight.

5.2.1 Estimating seed size using highlight translation

From discussions on shortcomings under section 2.1, Gnanaprakasam's work on seed height estimation from diffuse angle images [7] uses both primary and secondary / mirror highlight to estimate the height of seed defect from a single image. From experimental imaging, it was found that the primary highlight is prominent and remains unaffected even for smaller seed defects and for seed defects with paint pool at the base. This part of the thesis uses the discussion from section 5.2 to obtain useful information regarding the size of the seed. Consider the fig. 5.4. The different sized circles represent different seed sizes.

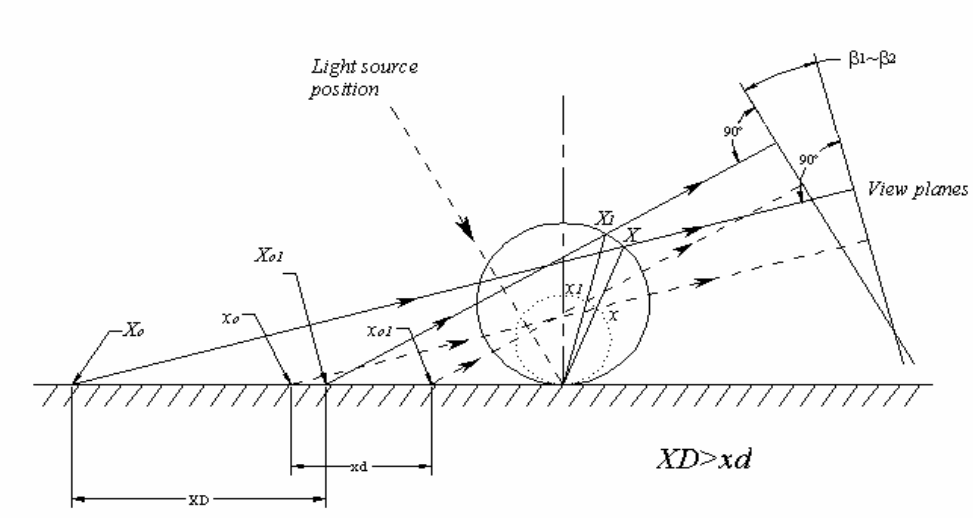

Fig. 5.4 Different seed sizes yield different translation

The images of seeds are captured under the same conditions, i.e. the light angle is at *'α'* and the camera angles are maintained at *'β_1'* for position 1 and *'β_2'* for position 2. As illustrated in fig. 5.4, for the larger seed the centroid of the highlight forms at points *'X_1'* and *'X'* for camera angles *'β_1'* and *'β'* respectively. This is recorded as the translation distance in the view plane bounded by points *'X_{o1}'* and *'X_o'* from where the light strikes the camera plane. The translation distance is this case is recorded as *'XD'*. Similarly for the smaller seed, the highlight forms at points *'x_1'* and *'x'* for camera angles *'β_1'* and *'β'* respectively. This is recorded as the translation distance in the view plane bounded by points *'x_{o1}'* and *'x_o'* from where the light strikes the camera plane. The translation distance in this case is recorded as *'xd'*. It can be noted that the translation distance due to larger seed, *'XD'* is less than its counterpart, *'xd'*. Similarly considering many seeds of varying diameter, it can be proved in similar fashion that as the size of the seed is increased, the translation distance also becomes correspondingly increased.

This increase in distance is due to the fact that the highlight centroids are enclosed within a constant sector of difference in highlight angles. The area of curvature enclosed within the same angle is more for a larger seed and less for a smaller seed. This is responsible for yielding greater translation distances when viewed by the camera.

5.2.2 Relationship between translation distance and size of seed defect:

Understanding the geometry of the seed and the location where the highlight gets formed over the surface of the seed provides a definite relationship between the size of the seed and the translated distance. The following discussion aims to establish such a relationship.

From fig. 5.1 and eqn. 5.1, the height of the seed highlight from the substrate is estimated to be:

$$h = r\left[1 + \cos\frac{\alpha - \beta}{2}\right]$$

The fig. 5.5 illustrates a seed defect over a specular surface; the position of the incident light source and the two camera positions at which the highlight formed over the seed are captured (β_1 *and* β_2). The points *'*X_{o1}*'* and *'*X_o*'* indicate the positions of the centroid of the highlight as viewed by the camera placed in the XY plane at the two camera angles respectively. The distance *'d'* is the translated distance of the highlight over the XY plane for these two camera angles. At camera angle *'*β_1*'*, let *'*e_1*'* denote the horizontal distance between projection of highlight on to the XY plane and the mapped location of the highlight as viewed by the camera and *'*h_1*'* denotes the height of the highlight from the stratum. Similarly *'*e_2*'* is the horizontal distance

and *'h_2'* is the height of the highlight from the stratum at camera angle *'β_2'*. From fig. 5.5, it can be shown that:

For position 1 of camera,

$$h_1 = r\left[1 + \cos\frac{\alpha - \beta_1}{2}\right]$$

$$e_1 = h_1 \tan\beta_1$$

$$z_1 = \frac{h_1}{\tan\left(90 + \frac{\alpha - \beta_1}{2}\right)} \Rightarrow z_1 = -h_1 \tan\left(\frac{\alpha - \beta_1}{2}\right)$$

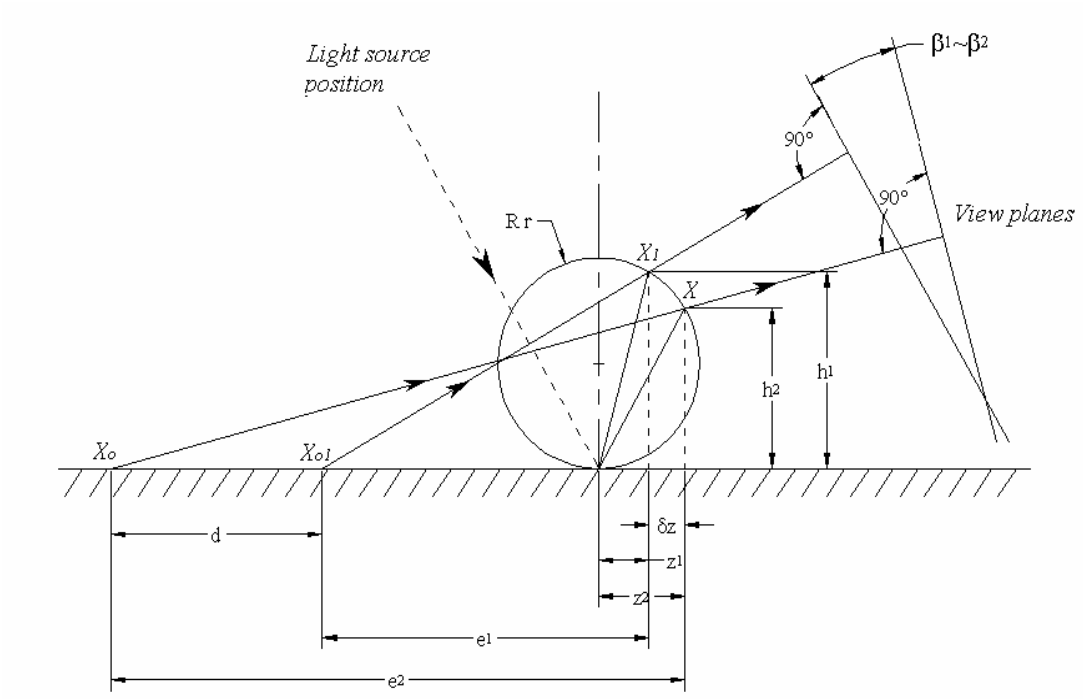

Fig. 5.5 Geometry for Highlight translation

For position 2 of camera,

$$h_2 = r\left[1 + \cos\frac{\alpha - \beta_2}{2}\right]$$

$$e_2 = h_2 \tan \beta_2$$

$$z_2 = \frac{h_2}{\tan\left(90 + \frac{\alpha - \beta_2}{2}\right)} \Rightarrow z_2 = -h_2 \tan\left(\frac{\alpha - \beta_2}{2}\right)$$

The translation distance can then be given by:

$d = e_2 - e_1 - \delta_z$, where

$$\delta_z = z_2 - z_1$$

Hence,

$$d = h_2 \tan \beta_2 - h_1 \tan \beta_1 + h_2 \tan\left(\frac{\alpha - \beta_2}{2}\right) - h_1 \tan\left(\frac{\alpha - \beta_1}{2}\right)$$

$$d = h_2\left[\tan \beta_2 + \tan\left(\frac{\alpha - \beta_2}{2}\right)\right] - h_1\left[\tan \beta_1 + \tan\left(\frac{\alpha - \beta_1}{2}\right)\right] \quad \text{….. 5.2}$$

Substituting the values of *'h_1'* and *'h_2'* in eqn. 5.2, reduces translation distance (d) as a function of single unknown variable the radius of the seed (r), and known variables light source angle (α) and camera angles at positions 1 and 2 (β_1 & β_2 respectively).

5.2.3 Approximation of translation distance

Simple and approximate height estimation is possible with the assumption that the highlights form at the top of seed [12]. This assumption can be used while working with images obtained from diffuse angles in Area 2 (fig. 3.3). This assumption requires modification in eqn. 5.2.

It can be noted that h_1 & h_2 are the height of the highlight from the base or stratum for camera angles β_1 *and* β_2 respectively. Based on the above assumption,

$$h_1 = h_2 = 2r \quad \text{….. 5.3}$$

Also, $\delta_z = z_2 - z_1$, where z_1 & z_2 are the horizontal projections of the highlight at two camera angles. Since the highlight is assumed to form always at the top, their projections are to the same point on the horizontal axis. Hence,

$$\delta_z = 0 \qquad \text{..... 5.4}$$

Substituting the eqn. 5.3 & 5.4 in eqn.5.2,

$$d = 2r\left(\tan\beta_2 - \tan\beta_1\right) \qquad \text{..... 5.5}$$

From the equation above the approximate radius of the seed can then be estimated. It is important to note that the relationship is independent of the angle of incidence. The estimation of translation distance in equations 5.2 and 5.5 can be found in Appendix B. Also submerged seeds are dealt with under Appendix C. The equations 5.2 and 5.5 derived in this section can be used to estimate the height of seed defect with only the primary highlight without the aid of highlight. The results from this discussion is expected to yield better accuracy in height estimation and quantify even smaller defect sizes compared to height estimation using multiple highlights [7].

5.3 Quantifying radius of seed defect

The highlight translation method proposed estimates the height of the seed. In order to distinguish the submerged seeds from superficial seeds and to encounter real world situation, it becomes very essential to estimate the radius of the seed. The radius of the seed or the surface area of the seed becomes very clearly evident when the images of the seed were captured at 0˚ of the camera, i.e. the optical axis of the camera being perpendicular to the plane of tile containing seeds. To filter out the shadow effect of the seed that forms when using the point light source at 30˚ angle, LED lighting of the camera was used. This sends out light at 0˚ to the vertical or at 90˚ to the tile plane.

The schematic of the set up for estimating the radius of the seed is shown in fig. 5.6. Estimating radius of seed defects usually is associated with an Edge-detection algorithm, which is time consuming when used in real-time instances (Appendix D). An alternate approach to estimate the radius or spread of seed defect would be to estimate the amount of area each pixel can capture in real world which can be utilized further for detecting radius. The following section is an attempt to recover the radius of seed defect with minimal image processing steps and time.

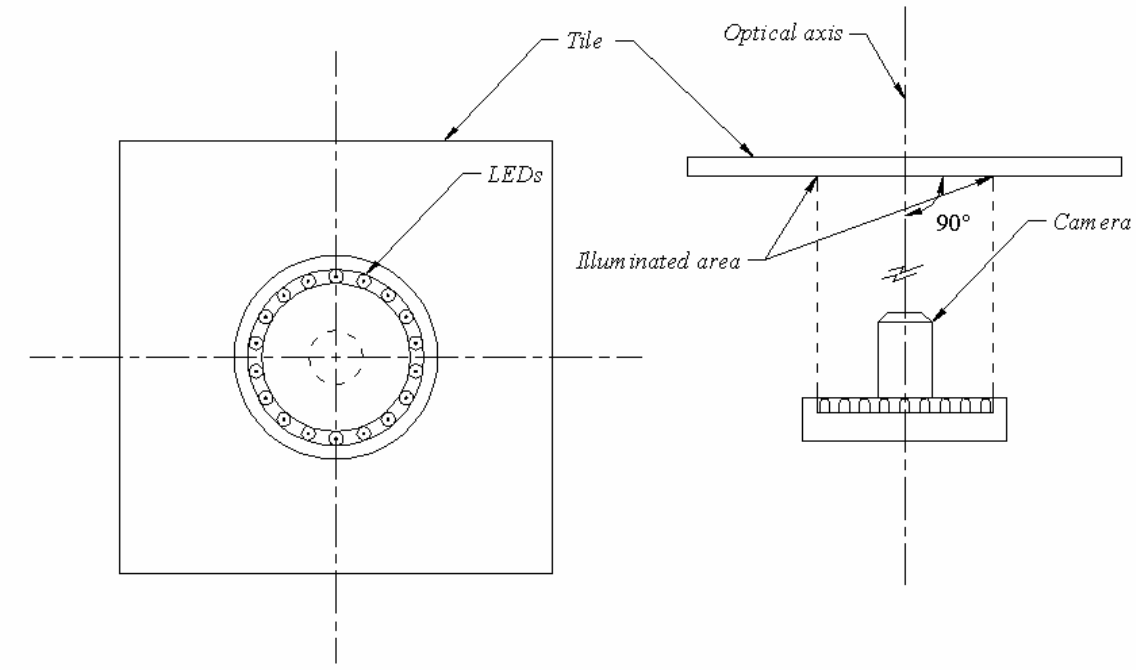

Fig. 5.6 Orientation of Tile and Camera for radius estimation

Area of the features due to seed defects can be easily obtained using any image processing software. The area obtained is in terms of pixels, i.e. the number of pixels enclosed within the area is obtained as output. It becomes very essential to convert this area into real world area in order to estimate the radius of seed defect.

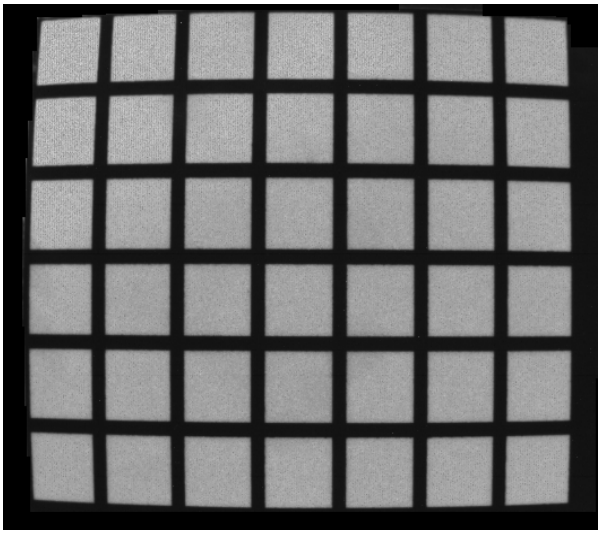

Fig. 5.7 Sample tile for area estimation

In order to determine a definite relationship between pixel area and real world area, a sample known is imaged at the same conditions as mentioned in section above, i.e. the camera is fixed at zero degrees and the illumination of the surface is brought about by the LEDs mounted in along side circumference of the camera itself. The target image is a retro reflective surface. Fig. 5.7 gives the sample tile that contains a 6x7 array of squares of equal area.

It can be noted that even though the real time area of squares are same in the array, the area obtained in pixels after thresholding the image appeared to vary much. The graphs presented in Fig. 5.8a & 5.8b indicate the change in area across rows and columns. Areas in pixels represent the number of pixels enclosed within each square in the sample tile.

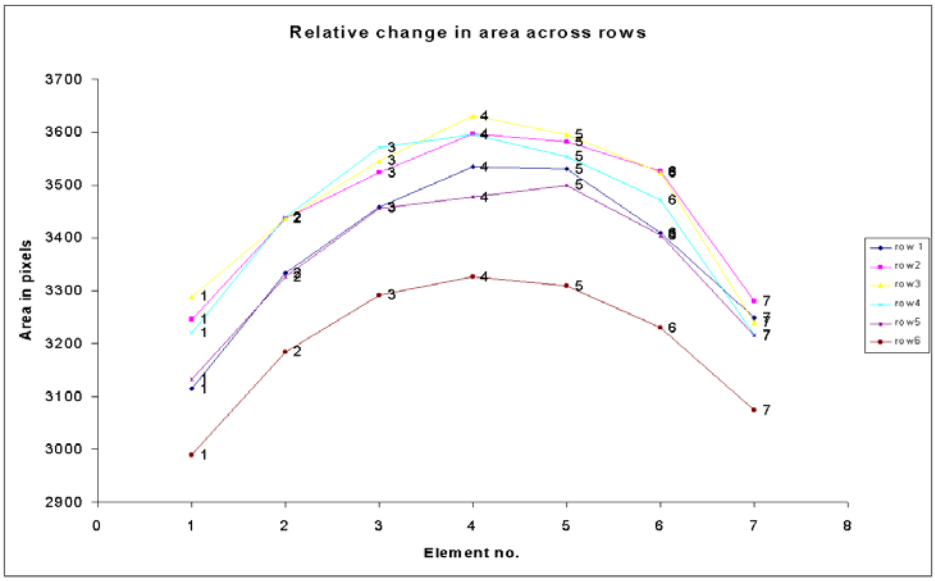

Fig. 5.8a Graph indicating variation in area on either side of center along rows

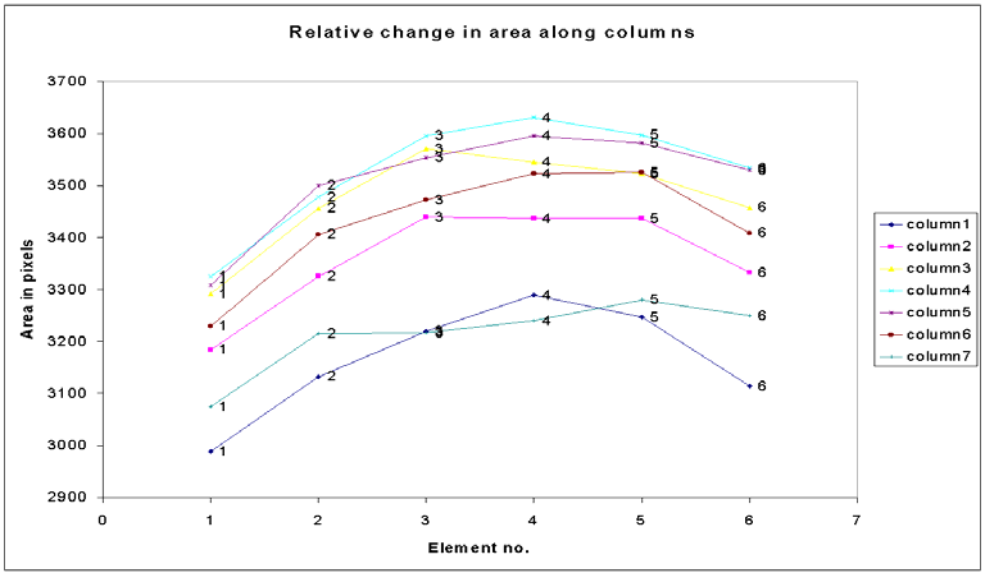

Fig. 5.8b Graph indicating variation in area on either side of center along columns

It can be inferred from the graph that the area of the features varies with a regular pattern on either side of the center of the image, i.e. a reduction in area can be observed on either side of the center. This reduction happens both along the row and

column of the plane of the image. This can be attributed to the distortion in the lens of the camera. Hence a direct linear relationship between the area in pixel and area in real time cannot be established. The following procedure could be adopted to obtain the area of a pixel. The procedure is described below:

1) A random camera co-ordinate *(XC1, YC1)* is picked within the image that is captured at 0°.

2) This can then be converted into real time co-ordinate *(WX1, WY1)* using calibration / interpolation.

3) Now an increment of a single pixel may be provided to the value of *XC1*, i.e. *XC2 = XC1 + 1*. (The co-ordinate now becomes *(XC2, YC2)* with *YC1 = YC2*).

4) The real time co-ordinate can then be estimated for this as *(WX2, WY2)*. (It is expected that the Y co-ordinate remains unaltered).

5) The difference between *WX1* and *WX2* gives the real world pixel distance in X-direction.

6) The steps 2 through 5 are carried out to determine the real world pixel distance in Y-direction.

However if these dimensions obtained are too small to realize, an arbitrary incremental value like 5,10,15… may be taken depending on the resolution obtained in real time co-ordinate. The subsequent area obtained may be of order 5x5, 10x10 or 15x15 pixels respectively. Assuming a linear relationship to exist, this may either be converted in terms of a single pixel or dealt as such as a pixel cluster. The image processing steps utilized for conversion of original image into final image (from

which area is derived) and a detailed explanation of this conversion from image co-ordinate to camera co-ordinate for images taken at 0˚ can be found in Appendix E.

Once the pixel value (*dxp, dyp*) in real time are known along X and Y direction, the amount of area the pixel captures in real world can be computed. The number of pixels (*N*) enclosed by the feature is obtained from an image processing software. Using '*N*', '*dxp*' and '*dyp*', the radius of the seed can be computed.

Area covered by single pixel in real world (A_p) = dxp x dyp

Number of pixels enclosed by the feature = N

Total area of the feature in real world = N x A_p

This area may then be equated to the area of a circle.

$$\pi r^2 = N \times dxp \times dyp$$

$$r = \sqrt{\frac{N \times A_p}{\pi}} \qquad \text{..... 5.6}$$

where '*r*' is the radius of the seed in real world.

One problem that could be encountered in thresholding is the actual area of the seed. A smaller thresholding value gives a larger area when compared to larger threshold and hence the accuracy of actual area of the seed might be lost in the process. However using the illumination in the camera, it can be noted that there is a sharp contrast between image features and the background (Fig. D.1). A sensible threshold value may be selected by trial and error for any known size of seed defect. This value may then be used for estimating the radius of seed defect.

5.4 Position of seed defect in real world co-ordinate

From fig. 5.4, the centroid of the highlight is not the actual location of the seed defect present in the substrate. The camera actually views the point X_o, which is the projection of the centroid of the highlight on the XY plane. Hence the actual position of the seed needs to be estimated.

From fig. 5.5 and from the discussions under the section 5.2.2, the following relations are obtained.

For any camera angle 'β',

$$h = r\left[1+\cos\frac{\alpha-\beta}{2}\right]$$

$$e = h\ \tan\beta$$

$$z = \frac{h}{\tan\left(90+\frac{\alpha-\beta}{2}\right)} \Rightarrow z_1 = -h\ \tan\left(\frac{\alpha-\beta}{2}\right)$$

where,

h – height of the centroid of highlight from substrate

e – distance between centroid of highlight and its vertical projection on the XY plane

z – distance between seed position and vertical projection of highlight center

Hence the distance of the seed from highlight center as seen by the camera on the xy plane is given by 'e-z' from the highlight centroid position 'X_o'.

Since the co-ordinate of the centroid of the highlight is known to be 'X_o', the following procedure is followed to estimate the exact location co-ordinate of the seed in the tile.

1) Estimate the centroid of the highlight.

2) Convert this into real world co-ordinate by calibrating the camera for known angle 'β' at which the image is captured.

3) Estimate the distance *'e-z'* with all the other known parameters

4) Subtract this distance from the real world X co-ordinate of point *'X_o'*. This gives the X co-ordinate of the seed position. The Y co-ordinate of the seed position is the same as the real world Y co-ordinate of the highlight centroid.

When the highlight of the seed is assumed to form at the top of the seed, the following procedure may be adopted. Consider the fig. 5.9 indicating the highlight on top of the seed. In this case, from eqn. 5.5, the parameter *'z'* ceases to exist and the distance *'e'* gets modified to *'e*(mod)*'*.

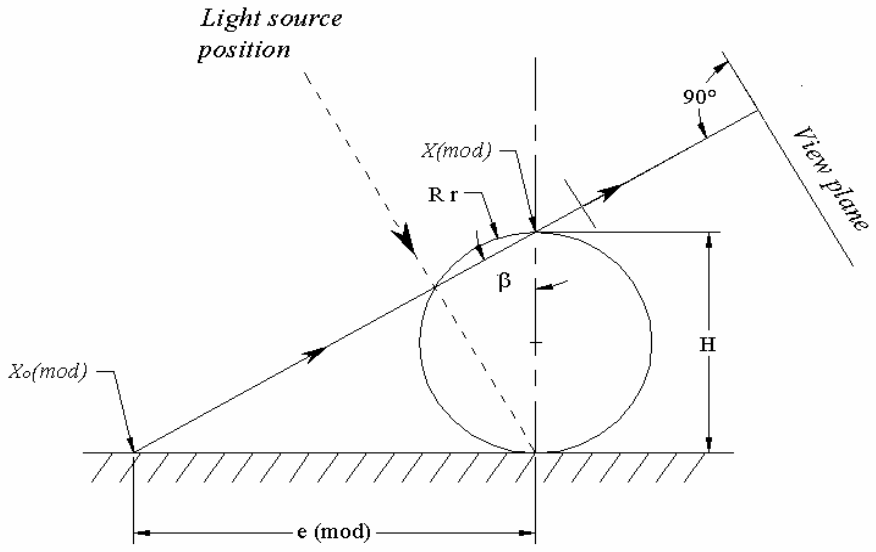

Fig. 5.9 Position of seed with highlight on top

The distance *'e*(mod)*'* in fig. 26 can be given by:

$e(\text{mod}) = H \tan \beta$

This distance can then be subtracted from the real world X co-ordinate of highlight centroid to obtain the exact location of the seed.

5.4.1 Aliter for seed location from seed and mirror highlight:

On the contrary to formation of a single highlight due to specular refection, a seed placed over highly reflective surface yields two highlights. The other highlight is due to mirror reflection of seed highlight by the highly specular surface [7,12]. The image of a seed captured at diffuse angle placed over a highly specular surface and the schematic of the mirror reflection and the subsequent capture of both highlights by the camera are presented in fig. 5.10.

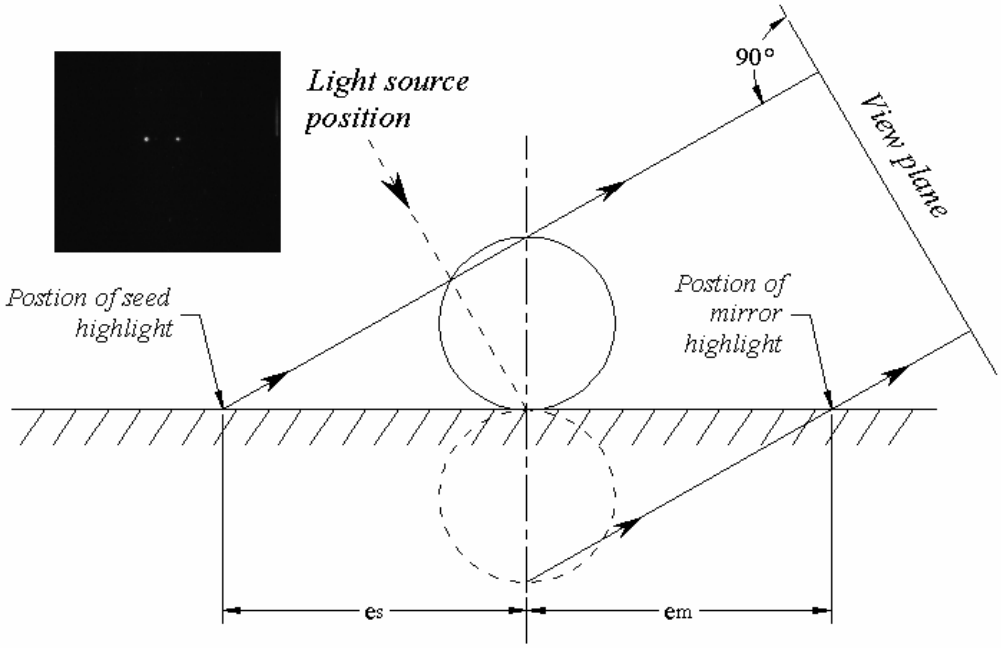

Fig. 5.10 Seed with mirror highlight and its corresponding schematic

From the seed geometry presented in fig. 5.10 it can be seen that the distance of the seed highlight and mirror highlight (formed due to specular base) from the center of the seed (e_s & e_m respectively) are same. Hence the following procedure may be followed to arrive at the position of the seed:

1) Read the image obtained at a known diffuse angle.
2) Estimate the centroid of the highlight and mirror highlight in pixel co-ordinates
3) Convert these pixel co-ordinates to real world co-ordinates by calibrating the camera for the known angle.
4) The mean of these co-ordinates gives the location of the seed.

Otherwise the mean of the pixel co-ordinates (highlight and mirror) may be estimated and then converted to real world co-ordinate to find the position of the seed.

CHAPTER SIX

INVESTIGATION ON CRATER DEFECTS

Another common type of surface defect is the crater defect. Dents on surfaces are characterized under these types of defects. Initial investigation to characterize craters in a manner similar to analytical expressions established for raised defects is presented in this chapter.

6.1 Studies on simulated crater defects

Fig. 6.1 gives the illustration of a hemispherical crater defect illuminated by a light source at an incidence angle of 30°. The path of the reflected ray is traced to the view plane positioned at a viewing angle of 70°. The Fig illustrates that a cluster of rays trace back to the view plane. This cluster forms a highlight to the left of the crater center.

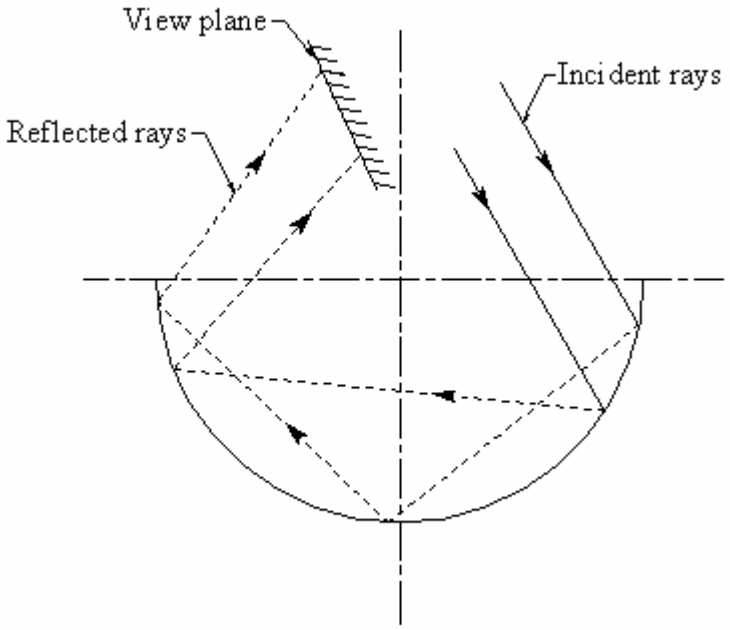

Fig. 6.1. Reflection from crater defect

In order to understand the location of highlight for various depths of crater, simulated images were generated using RADIANCE. The depths of the crater (h) were of order 1/8r, 2/8r, …. ,8/8r where 'r' is the radius of the crater defect. For initial investigation, the base of 8 was chosen to illustrate and categorize the depth with an accuracy of $1/8^{th}$ of unit length. Light source in simulation was at kept at angle 30˚ and camera was varied to obtain images at different angles. The angle of camera used was 50˚, 65˚ and 70˚.

6.1.1 Light at 30˚ and Camera at 50˚

The set of images obtained for camera angle at 50˚ with the incidence angle of light being 30° are presented in fig 6.2.

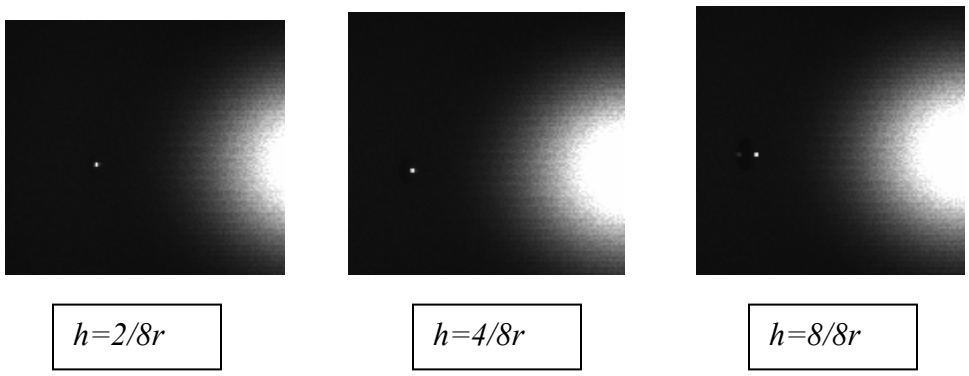

Fig.6.2. Images obtained at 50˚ indicating highlight positions for various depths

Key Observations:

- Single highlight spot to the right of crater center
- The distance of the highlight centroid from the center of the crater keeps increasing as the depth of the crater is increased

6.1.2 Light at 30˚ and Camera at 65˚: -

For a camera angle of 65˚ and various crater depths, the images obtained are presented in Fig 6.3.

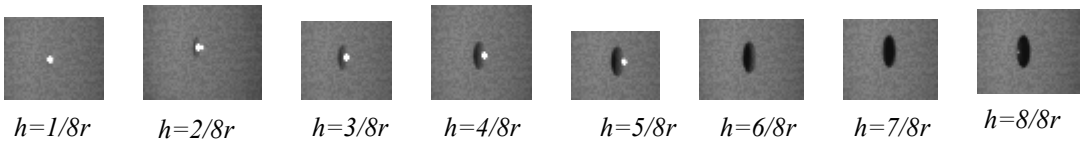

Fig. 6.3. Images obtained at 65˚ indicating highlight positions for various depths

Key Observations:

- Single highlight spot to the right of the crater center or no highlight spot
- The highlight floods the crater at very small depths (1/8 & 2/8r)
- The distance of the highlight centroid from the crater center keeps increasing as the depth of the crater is increased (3/8-5/8r)
- There is absolutely no highlight at 6/8r and 7/8r
- At h=8/8r, where the crater assumes the shape of hemisphere, the highlight shifts to the left of the crater centroid. No other crater depths possess this feature.

6.1.3 Light at 30˚ and Camera at 70˚: -

For a camera angle of 70˚ and various crater depths, the images obtained are presented in fig 6.4.

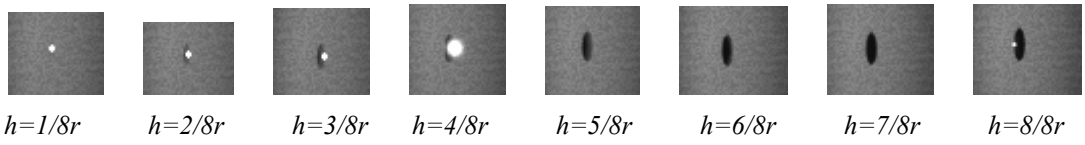

Fig. 6.4. Images obtained at 70˚ indicating highlight positions for various depths

Key Observations:

- Single highlight spot to the right of the crater center or no highlight spot

- The highlight floods the crater at very small depths (1/8 & 2/8r)
- The distance of the highlight centroid from the crater center keeps increasing as the depth of the crater is increased (3/8-5/8r)
- There is absolutely no highlight at 5/8,6/8 and 7/8r
- At h=8/8r, where the crater assumes the shape of hemisphere, the highlight shifts to the left of the crater centroid. No other crater depths possess this feature.

6.2. Conclusions from images:

From the key observations presented under section 6.1, with camera angle at 50˚, no rational conclusion could be drawn about the depth of the crater. Moreover the location of the highlight in the crater is also not known yet.

However with a camera angle of 65˚ and 70˚, the following conclusions could be made about the crater:

- Depending on the position of the highlight spot (left or right of the crater center), the depth of the crater with respect to its radius could be approximated.
- If the highlight spot is to the right of the crater center at cam angle 65˚, the range of depth can be predicted to be from 1/8 to 5/8r. However with additional image at 70˚, it can be noted that the range reduces to 1/8 to 4/8r (since an image with h=5/8r yields no highlight spot).
- Absence of highlight at 70˚ cam angle, suggests the range of depth to be within 5/8r and 7/8r. Again, the image at 65˚ cam angle reduces the range to 6/8r-7/8r if the highlight is absent and depth is approximately 5/8r if highlight were present in the image at that angle.

- Any highlight spot to the left of crater center at any of the angles 65˚ and 70˚ can be approximated to a crater with depth 8/8r or ‘h = r’ itself.

The table presented below summarizes the discussions.

Camera Angle - 65 degrees			**Camera Angle - 70 degrees**			**Predicted range**
Highlight position w.r.t. crater center			**Highlight position w.r.t. crater center**			
Left	**Right**	**Absent**	**Left**	**Right**	**Absent**	
Yes						8/8r or ‘r’
			Yes			8/8r or ‘r’
	Yes					1/8 – 5/8r
				Yes		1/8-4/8r
	Yes				Yes	5/8r
		Yes				6/8-7/8r
					Yes	5/8-8/8r

Table: 6.1. Predicted depth ranges for crater defects

An increase in resolution of the fractional ‘r’ increases the prediction accuracy of ratio between height and radius.

CHAPTER SEVEN

RESULTS AND DISCUSSIONS

This chapter presents the validity of relationships and theoretical models discussed in the previous chapters. The images used to validate are either real world or simulated images. The real world samples with defects are prepared as stated under section 3.1. Simulated seed defects on tiles were generated using the simulation software "RADIANCE". This is capable of simulating the real time seeds under the same conditions of ambience and other physical parameters. Images have been synthesized by using a Monte Carlo ray-tracer that uses Ward's light reflection model. This model is used mainly because it provides parameters that describe a range of measured real materials. Physically accurate image synthesis is a two-step process in which a physically accurate illumination simulation is followed by a mapping to pixel values based upon the imaging sensor. In the *Radiance* software, the surface material is characterized by material type, color, specular fraction and roughness. These parameters combined together can determine the three components of the reflection model - specular, directional diffuse and diffuse reflections. Using the predefined material, the test sample is modeled as a plane with defects on it.

The chapter summarizes the results obtained from introducing correction factor to Gnanaprakasam's hypothesis, results of height and position estimation using the proposed theory of highlight translation and the results of estimating seed radius using area of featured defect.

7.1 Correction factor for computed height using single image

Contrary to the assumption that the highlight forms on the top of the seed, it was shown in section 4.3 that the highlight forms at the bisection of camera angle and light source angle, the angle being measured from the center of the seed. The correction factor (χ) for the same is obtained from eqn. 5.1 which is:

$$\chi = \frac{h}{2r} = \frac{1}{2}\left[1 + \cos\frac{\alpha - \beta}{2}\right]$$

The image of the seed obtained had an incident angle (α) of 30˚ and camera angle (β) of 65˚. The correction factor is hence estimated to be:

$$\chi = \frac{h}{2r} = \frac{1}{2}\left[1 + \cos\frac{\alpha - \beta}{2}\right] = \frac{1}{2}\left[1 + \cos\frac{30 - 65}{2}\right]$$

$$\chi = 0.98$$

Hence the ratio of seed highlight height to the actual height of the seed can be given as:

$$\chi = \frac{h}{H} = 0.98$$

This factor is used to estimate the actual height of the seed. The height of the seed computed by Gnanaprakasam's hypothesis yields a height of *'h'*. This height is then multiplied with the reciprocal of correction factor ($1/\chi$) to obtain the actual height of the seed.

Sample Calculation:

A sample calculation is presented here. For a seed of height 1.9mm, the real world distance between the seed highlight and mirror highlight is calculated to be 7.66mm

Sl. No.	Seed height	Estimated first stage height	% Error	Estimated height after correction	% Error
1	1.70	1.53	10.03	1.57	7.90
2	1.80	1.60	11.28	1.63	9.18
3	1.90	1.79	6.03	1.83	3.81
4	2.40	2.04	15.00	2.09	12.99
5	2.10	2.02	4.02	2.06	1.75
6	1.90	1.69	11.11	1.73	9.00
7	1.80	1.61	10.63	1.65	8.51
8	3.10	2.80	9.58	2.87	7.45
9	2.40	2.12	11.51	2.17	9.42
10	1.70	1.48	12.78	1.52	10.72
11	1.80	1.68	6.68	1.72	4.47
12	2.00	1.81	9.67	1.85	7.53
13	2.00	1.90	4.98	1.95	2.73
14	1.80	1.71	5.26	1.75	3.02
15	1.70	1.62	4.42	1.66	2.16
16	2.00	1.82	8.85	1.87	6.69
17	1.70	1.61	5.37	1.65	3.13
18	1.70	1.59	6.76	1.62	4.55
19	1.80	1.67	6.99	1.71	4.80
20	1.90	1.79	5.77	1.83	3.54
21	2.10	1.90	9.76	1.94	7.62
22	2.00	1.90	4.82	1.95	2.56
23	2.00	1.80	10.11	1.84	7.98
24	2.10	1.96	6.75	2.00	4.54
25	1.70	1.53	9.73	1.57	7.59
26	1.70	1.65	2.95	1.69	0.65
27	1.90	1.68	11.82	1.72	9.73
28	1.80	1.68	6.91	1.72	4.70
29	1.90	1.78	6.17	1.82	3.95
30	1.40	1.31	6.31	1.34	4.10
31	1.70	1.61	5.06	1.65	2.82
32	1.70	1.53	9.71	1.57	7.58
33	7.50	6.97	7.09	7.13	4.89
34	5.90	5.35	9.25	5.48	7.10
35	4.00	3.64	9.00	3.73	6.85
36	3.10	2.80	9.66	2.87	7.53
		Avg. error	8.11%	Avg. error	5.93%

Table 7.1 Influence of correction factor on seed height correction

(from the image read and calibration). The seed height is then estimated using Pradeep's 3D characterization using single image. It is estimated to be:

$h = 1.79mm$

Now using the correction factorχ, the actual height of the seed is estimated to be:

$$H = \frac{h}{\chi} = \frac{1.79}{0.98} = 1.83mm$$

The percentage error in this case reduces from 6.04% to 3.8%. The influence of correction factor in seed height estimation depends on the angle of light source and camera angle. Having a narrow light source angle and a wider camera angle influences the estimated height to a large extent. The table 7.1 gives the estimated the height of the seed from the image and uses the correction factor to obtain the final height of the seed.

The average error in seed height estimation reduces by 26.9% from the original seed height obtained. The result obtained also confirms the fact that the seed highlight does not form on the top of the seed.

6.2 Seed height estimation using highlight translation

From section 5.2.2 on highlight translation, the following relations were obtained for a seed placed over the tile and illuminated with light angle *'α'* and the image captured at camera angle *'β_1 & β_2'*:

$$h_i = r\left[1 + \cos\frac{\alpha - \beta_i}{2}\right]$$

$$e_i = h_i \tan\beta_i$$

$$z_i = \frac{h_i}{\tan\left(90 + \frac{\alpha - \beta_i}{2}\right)} \Rightarrow z_i = -h_i \tan\left(\frac{\alpha - \beta_i}{2}\right)$$, where *'i' =1 or 2* depending on the position of the camera.

The translation distance can then be given by:

$d = e_2 - e_1 - \delta_z$, where

$\delta_z = z_2 - z_1$

The incident angle of light source is 30˚ and the image of the seed is captured by the camera at diffused angles 50˚ and 70˚. Hence,

$\alpha = 30°$
$\beta_1 = 50°$ &
$\beta_2 = 70°$

Hence, from the equations above, for camera position 1,

$$h_1 = r\left[1 + \cos\left(\frac{30 - 50}{2}\right)\right] = 1.99r$$
$$e_1 = 1.99r \times \tan 50 = 2.37r \quad \&$$
$$z_1 = -1.99r \times \tan\left(\frac{30 - 50}{2}\right) = 0.35r$$

for camera position 2,

$$h_2 = r\left[1 + \cos\left(\frac{30 - 70}{2}\right)\right] = 1.94r$$
$$e_2 = 1.94r \times \tan 70 = 5.33r \quad \&$$
$$z_2 = -1.94r \times \tan\left(\frac{30 - 70}{2}\right) = 0.71r$$

The distance 'δz' and translation distance'd' can then be estimated as:

$$\delta_z = 0.71r - 0.35r = 0.36r$$
$$d = 5.33r - 2.37r - 0.36r = 2.61r$$

Consider a seed height of 1.3mm. The images were captured at 50˚ and 70˚. The corresponding center co-ordinates of highlight were found to be 287.50, 203.00 & 301.33, 203.33 respectively. This co-ordinate is converted to real world co-ordinate by calibrating the camera at 50˚ and 70˚. The resultant real world co-ordinate was estimated to be 65.82, 71.94 & 64.12, 72.11 respectively. Since the translation along the Y direction is minimal, the translation along X direction is found to be:

$$d = 65.83 - 64.12 = 1.71mm$$

This translation distance is then equated to the above equation derived:

$$\text{i.e. } 2.61r = 1.71 \Rightarrow r = \frac{1.71}{2.61} = 0.66mm$$

The estimated height of the seed is therefore 1.31mm with an error percentage of 1.06%.

From table 7.2 it can be inferred that the average error in seed highlight estimation is 5.3%. The difference in height is attributed partly to error in camera calibration and centroid extraction. Also the translation model assumes the seeds to be circular in shape which is not true in practice, as the seeds are not perfectly circular or sometimes faceted. However the average error of 5.3% in real world images suggests that seeds do not have to be “perfect” for a very good approximation.

Sl. No.	Cam Ang	Highlight Loc		RW loc		Transl dist"d"	Est. ht	Actual height	% Error
		XCO	YCO	WXO	WYO				
	50	314.88	235.88	80.94	63.32				
1	70	308.50	236.00	76.70	63.32	4.23	3.25	3.60	9.83
	50	309.36	241.55	78.76	61.89				
2	70	302.00	241.80	71.86	61.88	6.90	5.29	5.00	5.82
	50	300.50	238.00	75.30	62.87				
3	70	293.17	237.83	65.08	63.04	10.22	7.84	7.80	0.47
	50	312.00	197.00	75.80	73.13				
4	70	314.67	197.33	74.07	73.22	1.73	1.33	1.30	2.23
	50	353.00	294.50	91.34	48.23				
5	70	337.33	294.67	89.54	48.22	1.80	1.38	1.30	6.21
	50	303.50	213.00	72.40	69.07				
6	70	310.00	213.50	70.66	69.10	1.74	1.34	1.30	2.75
	50	287.50	203.00	65.83	71.94				
7	70	301.33	203.33	64.12	72.11	1.71	1.31	1.30	1.06
	50	358.83	301.17	93.46	46.62				
8	70	341.17	301.83	92.00	46.54	1.46	1.12	1.30	14.06
	50	334.50	155.50	84.54	83.39				
9	70	328.00	155.00	83.41	83.55	1.13	0.87	1.00	13.28
	50	315.25	198.00	77.08	72.82				
10	70	316.83	197.83	75.62	73.01	1.46	1.12	1.10	1.80
	50	319.00	195.00	78.55	73.53				
11	70	319.00	194.50	77.16	73.79	1.39	1.07	1.00	6.64
	50	318.00	270.00	78.14	54.21				
12	70	318.50	270.50	76.80	54.07	1.35	1.03	1.00	3.18
	50	337.00	291.00	85.42	48.96				
13	70	329.00	291.50	84.04	48.84	1.38	1.06	1.00	5.73
	50	312.00	203.00	75.80	71.57				
14	70	318.50	203.00	76.81	71.60	1.01	0.77	0.80	3.40
	50	310.00	292.00	74.98	48.44				
15	70	317.00	292.00	75.73	48.44	0.75	0.57	0.60	4.67

Table 7.2 Results of Seed height estimation using Highlight translation

Sl. No.	Cam Ang	Highlight Loc		RW loc		Transl dist"d"	Est. ht	Actual height	% Error
		XCO	YCO	WXO	WYO				
	50	331.00	243.50	83.16	60.99				
16	70	329.00	243.00	84.04	61.12	0.89	0.68	0.60	13.45
	50	349.00	278.00	89.87	52.32				
17	70	339.00	278.50	90.61	52.26	0.74	0.57	0.60	5.46
	50	366.00	186.00	96.07	75.03				
18	70	349.00	185.00	96.94	75.02	0.87	0.67	0.60	11.18
	50	365.00	228.00	95.66	64.69				
19	70	348.00	227.00	96.28	64.86	0.62	0.48	0.50	4.59
	50	387.00	282.00	103.34	51.54				
20	70	361.00	283.00	104.06	51.47	0.73	0.56	0.60	7.21
	50	336.20	171.40	85.17	79.27				
21	70	324.75	171.00	81.18	79.62	3.99	1.53	1.50	1.95
	50	319.00	210.71	78.55	69.47				
22	70	315.50	210.50	74.67	69.74	3.88	1.49	1.50	0.77
	50	303.50	240.50	72.40	61.87				
23	70	307.00	240.50	68.43	61.97	3.97	1.52	1.50	1.46
	50	342.00	296.50	87.29	47.62				
24	70	328.33	296.67	83.59	47.51	3.70	1.42	1.50	5.44
	50	324.00	164.00	80.51	81.46				
25	70	316.50	164.00	75.38	81.90	5.12	1.96	1.85	6.17
	50	285.60	215.20	65.04	68.70				
26	70	296.50	215.00	60.35	69.08	4.69	1.80	1.85	2.73
	50	319.50	249.50	78.73	59.49				
27	70	314.33	249.33	73.82	59.58	4.91	1.88	1.85	1.77
	50	302.50	287.50	71.98	49.55				
28	70	305.00	287.50	66.91	49.37	5.06	1.94	1.85	4.93

Avg. error 5.29%

Table 7.2 Results of Seed height estimation using Highlight translation (Contd…)

Consider the correction factor for height estimation at angles 50˚ and 70˚. From the equation derived, the correction factor is given by:

$$\chi = \frac{h}{2r} = \frac{1}{2}\left[1 + \cos\frac{\alpha - \beta}{2}\right]$$

Hence, for camera angles 50˚ and 70˚, we have,

$$\chi_{50} = \frac{1}{2}\left[1 + \cos\frac{30 - 50}{2}\right] = 0.99$$
$$\chi_{70} = \frac{1}{2}\left[1 + \cos\frac{30 - 70}{2}\right] = 0.97$$

The value of the correction factor is close to 1. Hence for smaller seed defects the effect of this correction factor is negligible. The decision could be made using Fig. 5.2. It might very well be assumed that the seed highlight forms at the top of the seed. Applying the same in eqn. 5.5, the translation distance can be given by:

$$d = 2r(\tan\beta_2 - \tan\beta_1)$$
$$d = 2r(\tan 70 - \tan 50) \Rightarrow d = 3.11r$$

Sample Calculation:

Consider a seed radius of 3.3mm. The images were captured at 50˚ and 70˚. The corresponding center co-ordinates of highlight were found to be 298.16, 240.16 & 296.14, 239.71 respectively. This co-ordinate is converted to real world co-ordinate by calibrating the camera at 50˚ and 70˚. The resultant real world co-ordinate was estimated to be 91.06, 80.09 & 80.66, 80.25 respectively. Since the translation along the Y direction is minimal, the translation along X direction is found to be:

$$d = 91.06 - 80.66 = 10.40mm$$

From eqn. for translation distance,

$$2r(\tan 70 - \tan 50) = 10.40$$
$$r = 3.34mm$$

The estimated radius of the seed is therefore 3.34mm with an error of 1.34%. From table 7.3, the average error in estimating the size of the seed is 3.47%.

Sl. No.	Cam Ang	Highlight Loc		RW loc		Transl dist"d"	Est. ht	Actual height	% Error
		XCO	YCO	WXO	WYO				
	50	309.27	240.47	95.52	80.01				
1	70	307.19	240.43	89.76	80.05	5.76	1.85	1.80	2.92
	50	308.71	240.43	95.30	80.02				
2	70	306.50	240.50	89.21	80.03	6.09	1.96	2.00	2.09
	50	306.64	240.61	94.48	79.97				
3	70	305.50	240.50	88.41	80.03	6.06	1.95	2.10	7.18
	50	307.64	240.46	94.87	80.01				
4	70	304.50	240.61	87.61	80.00	7.26	2.34	2.20	6.15
	50	305.68	240.53	94.10	79.99				
5	70	302.67	240.50	86.12	80.03	7.97	2.56	2.50	2.55
	50	290.71	240.00	87.97	80.13				
6	70	288.88	240.13	74.23	80.14	13.74	4.42	4.50	1.81
	50	291.50	240.00	88.30	80.13				
7	70	288.88	240.13	74.23	80.14	14.07	4.52	4.40	2.82
	50	291.88	240.13	88.46	80.10				
8	70	289.50	240.00	74.80	80.18	13.66	4.39	4.30	2.15
	50	292.50	240.00	88.72	80.13				
9	70	290.50	240.00	75.70	80.17	13.02	4.19	4.20	0.33
	50	293.50	240.00	89.13	80.13				
10	70	291.25	240.00	76.37	80.17	12.76	4.10	4.10	0.09
	50	293.83	240.17	89.27	80.09				
11	70	291.50	240.00	76.59	80.17	12.68	4.08	4.00	1.92
	50	294.50	240.00	89.55	80.13				
12	70	292.50	240.00	77.48	80.17	12.07	3.88	3.90	0.51
	50	295.17	240.17	89.82	80.09				
13	70	293.50	240.00	78.36	80.17	11.46	3.69	3.80	3.01
	50	295.50	240.00	89.96	80.13				
14	70	294.00	240.00	78.80	80.17	11.16	3.59	3.70	3.00
	50	296.50	240.00	90.37	80.13				
15	70	294.50	240.00	79.23	80.17	11.14	3.58	3.60	0.52
	50	296.60	240.20	90.41	80.08				
16	70	295.50	240.00	80.10	80.17	10.31	3.32	3.50	5.26

Table 7.3 Results of Seed height estimation for simulated images

Sl. No.	Cam Ang	Highlight Loc		RW loc		Transl dist"d"	Est. ht	Actual height	% Error
		XCO	YCO	WXO	WYO				
	50	297.50	240.00	90.78	80.13				
17	70	296.25	240.00	80.75	80.17	10.04	3.23	3.40	5.09
	50	298.17	240.17	91.06	80.09				
18	70	296.14	239.71	80.66	80.25	10.40	3.34	3.30	1.34
	50	298.40	240.20	91.15	80.08				
19	70	297.60	240.20	81.90	80.12	9.25	2.98	3.20	7.04
	50	299.50	240.50	91.60	80.00				
20	70	298.40	240.20	82.58	80.12	9.02	2.90	3.10	6.41
	50	311.50	179.50	96.40	95.18				
21	70	310.00	179.71	91.97	95.52	4.43	1.42	1.50	5.04
	50	312.00	159.00	96.60	100.26				
22	70	310.20	159.40	92.13	100.68	4.47	1.44	1.50	4.26
	50	312.00	138.50	96.60	105.36				
23	70	310.00	139.00	91.98	105.90	4.62	1.48	1.50	1.05
	50	311.75	118.00	96.50	110.46				
24	70	310.33	118.67	92.24	111.04	4.26	1.37	1.50	8.78
	50	311.71	261.00	96.48	74.90				
25	70	310.00	260.71	91.95	74.88	4.53	1.46	1.50	2.83
	50	311.50	281.50	96.40	69.80				
26	70	310.00	281.29	91.94	69.64	4.45	1.43	1.50	4.53
	50	311.67	301.67	96.46	64.79				
27	70	310.00	301.29	91.94	64.54	4.52	1.46	1.50	3.03
	50	311.67	322.33	96.46	59.65				
28	70	310.00	322.00	91.93	59.26	4.53	1.46	1.50	2.93
	50	312.00	342.50	96.59	54.65				
29	70	310.25	342.00	92.12	54.19	4.47	1.44	1.50	4.18
	50	312.00	363.00	96.59	49.56				
30	70	310.33	362.33	92.18	49.02	4.41	1.42	1.50	5.46

Avg. error 3.48%

Table 7.3 Results of Seed height estimation for simulated images (Contd…)

7.3 Location of seed in view space

Simulated images generated using "RADIANCE" was used to estimate the location of the seed in the tile. The simulated images were used because the location of the seed in real world can be accurately known for verifying the results unlike the real time samples. From the algorithm presented in estimating the location of seed defect under section 5.4, it can be noted that the exact location of the seed can be given by:

$$X_s = X_o + (e - z) \;\&$$

$$Y_s = Y_o$$

where, (X_s, Ys) is the real world location of the seed

X_o is X co-ordinate of the highlight centroid in real world

Y_o is Y co-ordinate of the highlight centroid in real world

The value of 'e' and 'z' are given by the derivation in section 5.2.2. A sample calculation is presented below to estimate the location of the seed.

Let 'r' be the radius of the seed. Consider a seed placed at a real world location (100,80). The image of the seed is captured at a camera angle of 50˚ (β) with light source angle at 30˚ (α). The centroid of seed highlight is formed at pixel location (311.5, 240.5). This is converted to real world co-ordinates by calibrating the camera at 50˚. The estimated real time location of the centroid of seed highlight is (96.4,80.0). Now the parameters *'h', 'e'* and *'z'* are estimated from the formulae below:

$$h = r\left[1+\cos\frac{\alpha-\beta}{2}\right] = 1.5\times\left[1+\cos\frac{30-50}{2}\right] = 2.98$$

$$e = h\ \tan\beta = 2.98\times\tan 50° = 3.55$$

$$z = -h\ \tan\left(\frac{\alpha-\beta}{2}\right) = -2.98\times\tan\left(\frac{30-50}{2}\right) = 0.53$$

The real time X and Y co-ordinate of the seed is given by:

$$X_s = X_o + (e - z)$$
$$X_s = 96.40 + (3.55 - 0.53) = 99.42$$
$$Y_s = Y_o = 80.00$$

The Y co-ordinate of the seed remains the same as the highlight because the translation along the direction is minimal and can be ignored. Hence the estimated location of the seed in real time is given by (99.42, 80.00) with the exact location being (10, 80). This error in estimating the seed location is 0.58% for X co-ordinate and 0% for Y co-ordinate. The tables 3 & 4 gives the location of seed in tile space for images captured with two different camera angles 50˚ and 70˚ respectively.

An average error of 0.69% and 1.15% for ‘X’ and 1.01% for ‘Y’ is observed for camera angles 50˚ and 70˚ respectively. The increased error for camera angle at 70˚ can be attributed to the increased normalized error during camera calibration for larger angles.

Sl. No.	Highlight		Seed highlight		h	e-z	Estimated		Actual	
	XCO	YCO	WXO	WYO			X	Y	X	Y
1	311.5	240.5	96.4	80.0	3.0	3.0	99.4	80.0	100.0	80.0
2	368.5	240.5	116.9	80.0	3.0	3.0	120.0	80.0	119.1	80.0
3	384.0	240.5	121.9	80.0	3.0	3.0	125.0	80.0	125.4	80.0
4	400.3	240.7	127.0	80.0	3.0	3.0	130.0	80.0	131.8	80.0
5	263.5	240.5	76.0	80.0	3.0	3.0	79.1	80.0	81.0	80.0
6	253.0	240.5	71.1	80.0	3.0	3.0	74.2	80.0	74.6	80.0
7	242.5	240.5	66.1	80.0	3.0	3.0	69.1	80.0	68.3	80.0
8	311.7	220.3	96.5	85.0	3.0	3.0	99.5	85.0	100.0	86.4
9	311.8	199.8	96.5	90.1	3.0	3.0	99.6	90.1	100.0	92.7
10	312.0	159.0	96.6	100.3	3.0	3.0	99.6	100.3	100.0	99.1
11	312.0	138.5	96.6	105.4	3.0	3.0	99.6	105.4	100.0	105.4
12	311.8	118.0	96.5	110.5	3.0	3.0	99.5	110.5	100.0	111.8
13	311.7	261.0	96.5	74.9	3.0	3.0	99.5	74.9	100.0	73.7
14	311.5	281.5	96.4	69.8	3.0	3.0	99.4	69.8	100.0	67.3
15	311.7	322.3	96.5	59.7	3.0	3.0	99.5	59.7	100.0	61.0
16	312.0	342.5	96.6	54.7	3.0	3.0	99.6	54.7	100.0	54.6
17	312.0	363.0	96.6	49.6	3.0	3.0	99.6	49.6	100.0	48.3

Avg. error in estimating X co-ordinate = 0.69% and Y co-ordinate = 1.01%

Table 7.4 Results of Seed Location for 50˚ camera angle

Sl. No.	Highlight		Seed highlight		h	e-z	Estimated		Actual	
	XCO	YCO	WXO	WYO			X	Y	X	Y
1	310	240.7	91.953	79.977	2.9	6.9	98.89	79.98	100	80
2	339.8	240.4	112.73	80.048	2.9	6.9	119.7	80.05	119.1	80
3	348.5	240.5	118.04	80.023	2.9	6.9	125	80.02	125.4	80
4	357.5	240.5	123.22	80.022	2.9	6.9	130.2	80.02	131.8	80
5	285.5	240.5	71.116	80.039	2.9	6.9	78.05	80.04	80.95	80
6	280.5	240.5	66.344	80.04	2.9	6.9	73.28	80.04	74.6	80
7	275	240.5	60.862	80.042	2.9	6.9	67.8	80.04	68.25	80
8	310	220.3	91.958	85.184	2.9	6.9	98.89	85.18	100	86.35
9	309.9	199.9	91.866	90.39	2.9	6.9	98.8	90.39	100	92.7
10	310.2	159.4	92.128	100.68	2.9	6.9	99.06	100.7	100	99.05
11	310	139	91.979	105.9	2.9	6.9	98.91	105.9	100	105.4
12	310.3	118.7	92.242	111.04	2.9	6.9	99.18	111	100	111.8
13	310	260.7	91.948	74.88	2.9	6.9	98.88	74.88	100	73.65
14	310	281.3	91.943	69.637	2.9	6.9	98.88	69.64	100	67.3
15	310	322	91.934	59.262	2.9	6.9	98.87	59.26	100	60.95
16	310.3	342	92.122	54.19	2.9	6.9	99.06	54.19	100	54.6
17	310.3	362.3	92.182	49.024	2.9	6.9	99.12	49.02	100	48.25

Avg. error in estimating X co-ordinate = 1.15% and Y co-ordinate = 1.01%

Table 7.5. Results of Seed Location for 70˚ camera angle

7.4 Radius of the seed defect

As discussed in section 5.3, to estimate the radius of the seed, the image is captured at 0˚ with self-illumination of the camera. The radius of the seed is given in real time by equation 5.6. If *'r'* is the radius of the seed then,

$$r = \sqrt{\frac{N \times A_p}{\pi}}$$

where N – total number of pixels enclosed by feature

A_p – Area of pixel in real time

The average area of pixel in real world is estimated to be 0.27x0.27 mm^2. (Appendix E). The number of pixels enclosed by the feature is found using the Image processing toolbox in MATLAB. The radius is then estimated by the formula given in equation 5.6. For an image of a tile captured at zero degrees, the number of enclosed pixels for a seed feature was 89. Hence N=89. The radius of the seed is then given as:

$r = \sqrt{\frac{89 \times 0.27 \times 0.27}{\pi}} = 1.44mm$, the actual radius being 1.4mm and with an error percentage of 2.65%.

Sample images of different tiles were captured and their results are presented in table 7.6.

Sl.	Threshold	Area	Area in real	Est	Actual	%
1	110	94	6.85	1.48	1.40	5.49
2	110	87	6.34	1.42	1.40	1.49
3	110	89	6.49	1.44	1.40	2.65
4	110	82	5.98	1.38	1.40	1.47
5	110	75	5.47	1.32	1.40	5.77
6	110	86	6.27	1.41	1.40	0.90
7	110	139	10.13	1.80	1.90	5.48
8	110	149	10.86	1.86	1.90	2.14
9	110	263	19.17	2.47	2.40	2.93
10	110	267	19.46	2.49	2.40	3.71
11	110	229	16.69	2.31	2.40	3.95
12	110	243	17.72	2.38	2.40	1.06
13	110	232	16.91	2.32	2.40	3.32
14	110	236	17.20	2.34	2.40	2.49
15	110	238	17.35	2.35	2.40	2.08
16	110	176	12.83	2.02	2.00	1.05
17	110	171	12.47	1.99	2.00	0.40
18	110	190	13.85	2.10	2.00	4.99
19	110	154	11.23	1.89	2.00	5.48
20	110	186	13.56	2.08	2.00	3.88
21	110	175	12.76	2.02	2.00	0.76
22	110	203	14.80	2.17	2.00	8.52
23	110	172	12.54	2.00	2.00	0.11
24	110	164	11.96	1.95	2.00	2.46
25	110	182	13.27	2.06	2.00	2.75
26	110	163	11.88	1.95	2.00	2.76
27	110	236	17.20	2.34	2.40	2.49
28	110	225	16.40	2.29	2.40	4.79
29	110	257	18.74	2.44	2.40	1.75
30	110	272	19.83	2.51	2.40	4.68
31	110	231	16.84	2.32	2.40	3.53
32	110	222	16.18	2.27	2.40	5.43
33	110	241	17.57	2.37	2.40	1.47
34	110	238	17.35	2.35	2.40	2.08
35	110	264	19.25	2.48	2.40	3.13
36	110	266	19.39	2.48	2.40	3.52
37	110	222	16.18	2.27	2.40	5.43
38	110	228	16.62	2.30	2.40	4.16
39	110	238	17.35	2.35	2.40	2.08
40	110	253	18.44	2.42	2.40	0.96
41	110	262	19.10	2.47	2.40	2.74
42	110	227	16.55	2.30	2.40	4.37
				Avg. error		**3.11%**

Table 7.6 Results of Seed radius estimation for real time images

From table 7.6, it can be observed that the average error percentage in seed radius determination using area is around 3.112%. Hence, the radius of the seed can be determined from area of the feature without actually having the necessity to use a circle-fitting algorithm and fit a best circle for the feature to know the size of a spherical seed. This eliminates processing time due to image processing and circle-fitting.

CHAPER EIGHT

CONCLUSION AND RECOMMENDATION FOR FUTURE WORK

8.1 Conclusion

A robust inspection methodology for detecting and quantifying a particular type of defect - seed defect has been presented in the thesis. The use of diffuse angles to obtain high contrast images that can quickly be used to obtain consistent information pertaining to seed defect has been demonstrated. The thesis also presented a two dimensional analytical approach to explain the phenomenon of highlight formation and its exact location given the light source and camera angle.

Another significant achievement of the work involves the estimation of correction factor for the proposed hypothesis of characterizing the seed defect using a single image. The presence of secondary highlight in mirror like surfaces cannot always be used to quantify seed defects because of the presence of paint pool in smaller seeds. The thesis provides a way out of this problem by formulating the theory of highlight translation. The primary highlight / seed highlight that follows this theory was utilized for estimating the height of the seed. As an outcome of this theory, the actual location of the seed could also be estimated in real time without having the necessity to capture an additional image at zero degrees.

The work also proposes to estimate the radius of seed defects without using complex edge-detecting algorithms. The proposed approach, which directly converts the area of seed defects to its radius using a zero degree real world conversion of image co-ordinates, involves very minimal and basic image processing techniques and hence reduces processing time.

The work therefore characterizes a seed defect completely by quantifying all the parameters that constitute a seed defect – height, radius and position. The results obtained in all these categories are found to be highly accurate with an error percentage of less than 5% in almost all cases.

The thesis has also addressed another common type of defect – the crater defect and has formulated a table to predict the height / radius ratio of crater defects from the highlight information derived from crater images.

8.2 Recommendations for future work

- The image processing computations are currently carried out separately. This could very well be incorporated in the DVT sensor for online quantification.
- The seed defects considered for the work were all placed on a smooth flat stratum. The work could be extended to surfaces that are curved which may very well simulate real time situations.
- The base tiles used for conducting experiments were painted black in all cases. Different colored tiles with seed defects could be used for studies to help understand the sufficiency of contrast in gathering information.
- Seeds of very small sizes in real time can be used by increasing the zoom level of the camera used for capturing the seed highlight.
- Characteristic of highlights for other shapes of defects – parabolic or elliptical may assist in encapsulating all types of real time seed defects.
- Utilizing a diffuse light source for estimating radius of the seed defects covers a larger area than a direct light source (currently used) from the camera. This might improve the speed of inspection by covering larger areas at one time.

- The research was conducted on tiles that were painted with solid color paint. Other types of paints like metallic, pearlescent and combination paints can be used for future study to understand off-specular reflections from such surfaces.
- Crater defects were all simulated for analysis purposes. A sample tile with crater defects could be used for comparing the results obtained in real time with simulated images.
- Finer classification of defects on a base of 16 could be used to further increasing the accuracy of prediction of crater defects.

APPENDIX A

PARAMETERS IN EXPERIMENTAL SETUP

A.1 Divergence of Light source

The light source used in the setup is divergent. The divergence angle need to be determined because the incident angle of the light source striking the seed defect at any point in the illuminated area of the tile changes with reference to the position where the seed is positioned. The maximum illuminated diameter (*D*) and the minimum diameter (*d*) of the illuminated area of light source are measured. These are measured by placing a tile in the experimental test bed in the position where images are captured and at a position as close as possible to the light source respectively. Consider the fig. A.1 representing the divergent source of light used in the set-up.

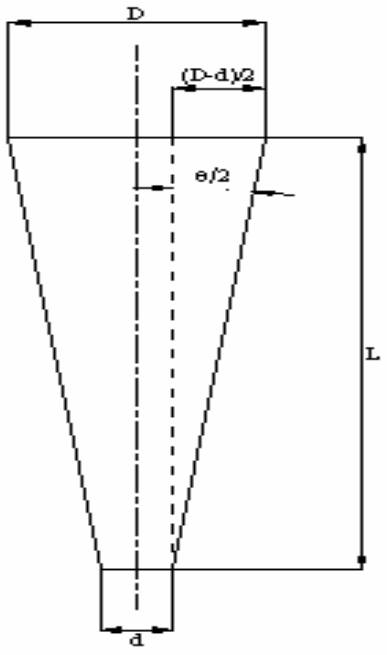

Fig. A.1 Divergence of light source

Let d – minor diameter near the light source

D – major diameter where the light strikes a surface

L – distance between source and object

From fig. A.1,

$$\tan\frac{\theta}{2} = \frac{D-d}{2L} \Rightarrow \frac{\theta}{2} = \tan^{-1}\frac{D-d}{2L}$$

Therefore, the angle of divergence is given by:

$$\theta = 2\ \tan^{-1}\frac{D-d}{2L}$$

A.2 Extended Point source of Light:

Now the central ray of light from the light source strikes a fixed point always. Camera's position along its circular path has its center always at this point. The fixed point is referred to as the Origin *O*. To be used for further calculation purposes, the extended point source of light, *'A'* needs to be determined. In order to obtain this, both the hypotenuse in fig. A.1 forming an angle of *θ/2* degrees with the vertical are extrapolated to meet the central vertical line. Because of the symmetry, all these three lines intersect at a single point that represents a point light source for the set-up. This is represented in fig. A.2.

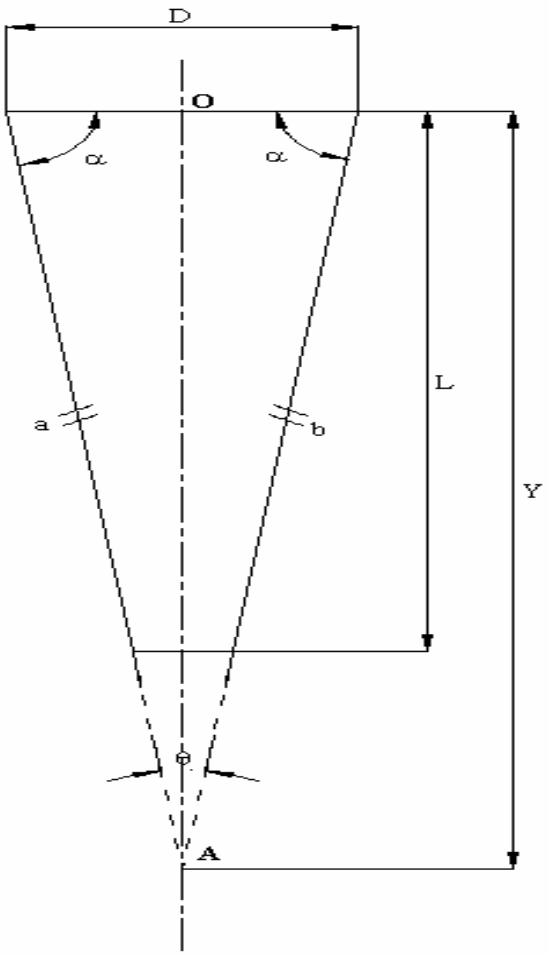

Fig. A.2 Extended point light source

Let *'a'* and *'b'* be the distance of the extreme rays of light from the point on the surface to the extended light source

From the Fig,

$a = b$ for 0° light source angle &

$$\alpha + \alpha + \theta = 180^\circ \Rightarrow \alpha = 90 - \frac{\theta}{2}$$

$$\frac{D}{\sin\theta} = \frac{a}{\sin\alpha} = \frac{b}{\sin\alpha}$$

Hence

$$a = b = \frac{D \sin \alpha}{\sin \theta}$$

Let the fixed point of center of strike of light source be assumed to have the co-ordinates of origin (0,0) and let 'Y' be the perpendicular distance between the points A & O. The co-ordinate of the assumed point source can then be estimated as follows:

$$Y = \sqrt{\frac{D^2 \sin^2 \alpha}{\sin^2 \theta} - \frac{D^2}{4}} = \frac{D}{2 \sin \theta} \sqrt{4 \sin^2 \alpha - \sin^2 \theta}$$

New location of assumed point source:

The light source is now rotated through a certain angle 'γ' with respect to the vertical. The rotation of light source causes the extended point source to be shifted from *'A'* to a new position *'A_x'*. Refer Fig. A.3.

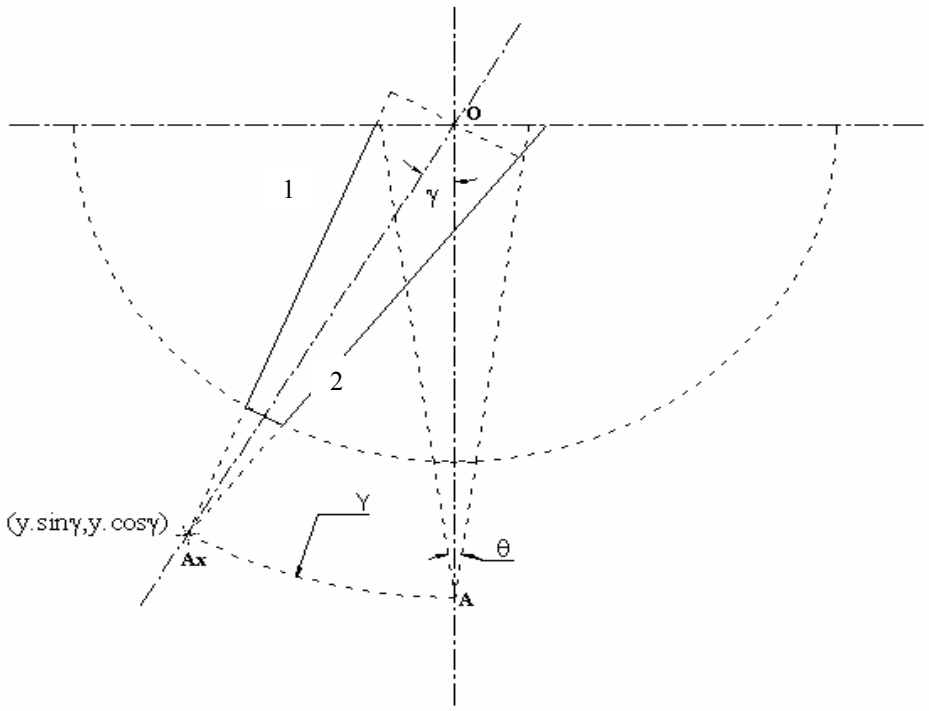

Fig. A.3 New location of assumed point source

The co-ordinates of this new location 'A_x' is given by:

X – co-ordinate = Y sinγ &

Y – co-ordinate = Y cosγ ….. A-1

Estimation of maximum area of illumination:

It is necessary to estimate the maximum area of illumination in order to determine the area over the painted surface that can be viewed by the camera. The area of illumination is a direct contributor to the speed with which the inspection can be carried out in real time paint body inspection.

Since the camera angle is varied in only one direction, the resultant area of illumination is an ellipse with minor axis being insignificantly different from the original diameter of the circular illumination obtained at 0˚. Hence it is sufficient to estimate just the major axis length of the illuminated ellipse.

In order to estimate the illuminated area, the equation of line in general form: "*y=mx+c"* is used, where,

m - slope of the line with X-axis

c - Y intercept

Fig. A.3 indicates the illuminated area of light source at angle 'γ'. The extreme possible light rays are numbered 1 & 2.

Angle of ray 1 with X-axis = $90 - \gamma + \frac{\theta}{2}$

Slope of ray 1 = m_1 = $\tan\left[90 - \left(\gamma - \frac{\theta}{2}\right)\right] = \cot\left(\gamma - \frac{\theta}{2}\right)$

Similarly,

Angle of ray 2 with X-axis = $90 - \gamma - \frac{\theta}{2}$

Slope of ray 2 = m_2 = $\tan\left[90 - \left(\gamma + \frac{\theta}{2}\right)\right] = \cot\left(\gamma + \frac{\theta}{2}\right)$

Equation of ray1 slope-intercept form is given by:

$y = m_1 x + c_1$ ….. A-2

The co-ordinate of the point source at camera angle γ is given by equation A-1. Substituting the values of X and Y co-ordinates in equation A-2 gives:

$$Y\cos\gamma = \cot\left(\gamma - \frac{\theta}{2}\right) \times Y\sin\gamma + c_1$$

Therefore,

$$c_1 = Y\left[\cos\gamma - \sin\gamma\cot\left(\gamma - \frac{\theta}{2}\right)\right]$$

Hence the equation of the ray1 is given by:

$$y = x\cot\left(\gamma - \frac{\theta}{2}\right) + Y\left[\cos\gamma - \sin\gamma\cot\left(\gamma - \frac{\theta}{2}\right)\right] \quad \text{….. A-3}$$

To obtain the point where the light ray 1 strikes the reflected surface, put y = 0 in the above equation.

$$x_1 = \frac{-Y\left[\cos\gamma - \sin\gamma\cot\left(\gamma - \frac{\theta}{2}\right)\right]}{\cot\left(\gamma - \frac{\theta}{2}\right)} \quad \text{….. A-4}$$

where $(x_1, 0)$ is the co-ordinate of ray1 at the reflected surface.

Similarly for ray 2, the co-ordinate where the ray 2 strikes the reflected surface is estimated and is given by:

$$x_2 = \frac{-Y\left[\cos\gamma - \sin\gamma \cot\left(\gamma + \frac{\theta}{2}\right)\right]}{\cot\left(\gamma + \frac{\theta}{2}\right)} \qquad \text{….. A-5}$$

From equations A-4 and A-5, the illuminated area can be estimated. The major axis length of the illuminated elliptical area is given by:

Major axis length = $\sqrt{(x_1 - x_2)^2}$ &

Minor axis length = D, the diameter of illuminated area at 0˚.

APPENDIX B

ESTIMATION OF TRANSLATION DISTANCE

The eqns. 5.2 & 5.5 are used to estimate the size of the seed defects. This requires the value of 'd', the translation distance, for estimation. In order to estimate the translation distance'd' from the images, the following procedure is adopted with assistance of MATLAB:

1) The image of the tile obtained at 50˚ and 70˚

2) Preliminary image processing (Image subtraction) to eliminate source reflection may be required for the image captured at 50˚ angle

3) The centroid of the seed highlight is then estimated for each image, the co-ordinates of the centroids are now obtained in terms of pixel

4) The pixel co-ordinate of each centroid is then converted to real world pixel co-ordinates using Tsai's Calibration procedure

5) The difference in real world distance between the two centroids of images gives the translation distance, '*d*'

6) The distance obtained is used in eqns. 5.2 or 5.5 to extract size information of seeds.

APPENDIX C

SUBMERGED SEEDS

A seed defect is completely quantified, provided the following information about the seed is known. The defects under study are constrained to spherical seeds. Hence the following parameters need to be determined to quantify a spherical seed completely. They include:

- Height of the seed defect
- Radius of the seed defect &
- Position of the seed defect

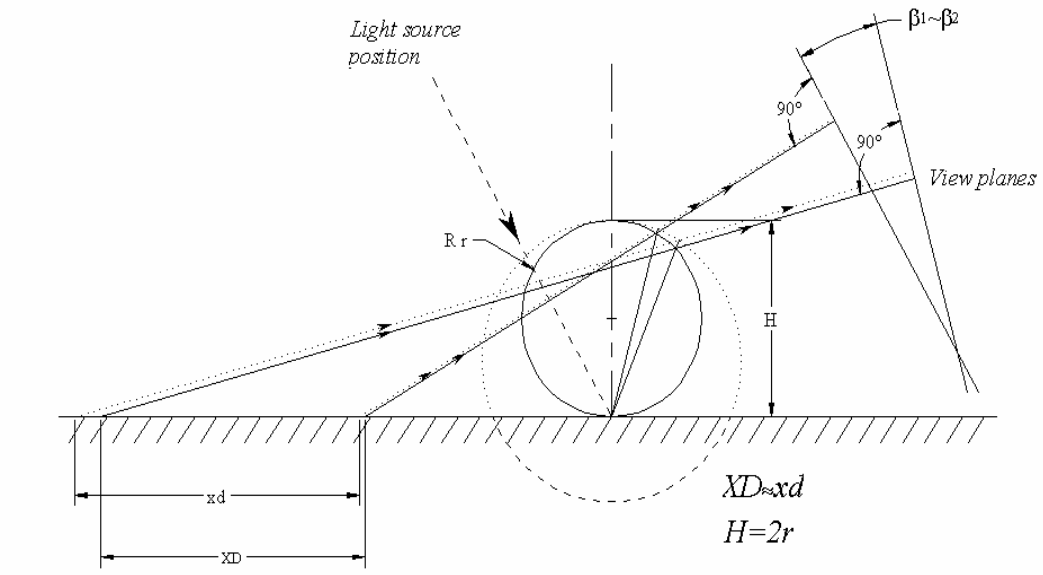

Fig. C.1 Difference in translation distance of a submerged and superficial seed

The method of highlight translation discussed in the previous sections treats the seed as if they are superficially positioned. Hence the radius obtained using eqns. 5.2 & 5.5 are either the radius of the seed (if they are superficial) or the maximum radius of a

superficial seed whose height could be fit within a submerged seed. The following illustration explains this.

Fig. C.1 indicates a submerged seed with height *'H'* and a superficial seed with radius *'r'* and height '*2r'*. The seed centers of both the seeds in the XY plane are the same. Now the highlights of these seeds are captured at angles *'β_1'* and *'β_2'*. Applying the phenomenon of highlight formation and translation, their corresponding centroids and translation distance are computed using the algorithm presented above. It may be found that in both the cases the translation distance approximately remains the same. (For example, a superficial seed with 1.8 mm radius and a submerged seed with 2.6 mm radius yield a translation distance of 5.3 mm and 5.7 mm respectively)

Since in both the cases, the translation distance is the same, and that the eqns. 5.2 & 5.5 are just function of the radius of the seed (keeping other parameters constant), the resultant radius in both the cases are approximately the same, which is not true. Hence the model proposed gives the radius of the seed if the seeds were superficial, but provides the same radius as the superficial seed if fitted within the submerged seed. Therefore the model presented may be used as a tool to estimate the height of the seed whose value does not vary for either a superficial seed or a fitted submerged seed.

APPENDIX D

RADIUS USING EDGE DETECTION ALGORITHM

The image captured using the set up shown in Fig 5.6 is presented in fig D.1. Fig shows five seed defects randomly positioned on the tile space.

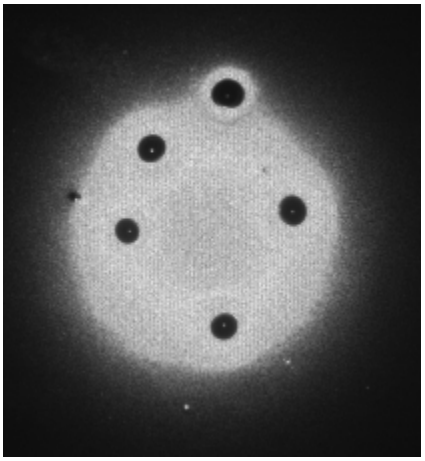

Fig. D.1 Seeds captured at 0˚ camera angle using self-illumination

This image is then processed using the image processing toolbox of MATLAB. The evolution of the final image is shown pictorially in fig. D.2. The final image is arrived at by performing various basic image-processing techniques like thresholding, morphological cleaning of image, edge detection and image subtraction.

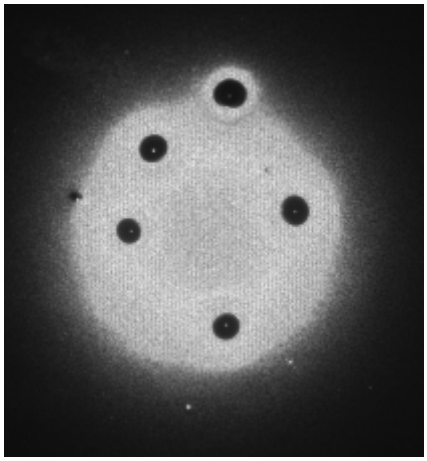

Step 1. Original Image captured by camera at 0˚ angle using self-illumination

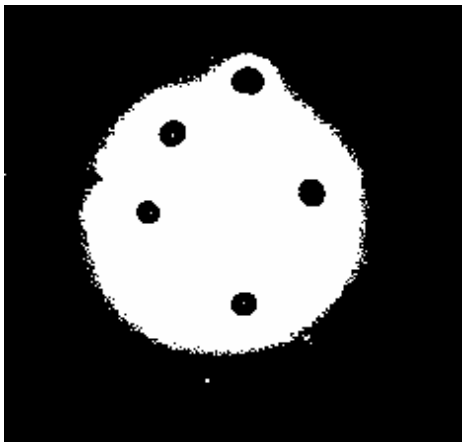

Step 2.Thresholded image at threshold intensity of 100

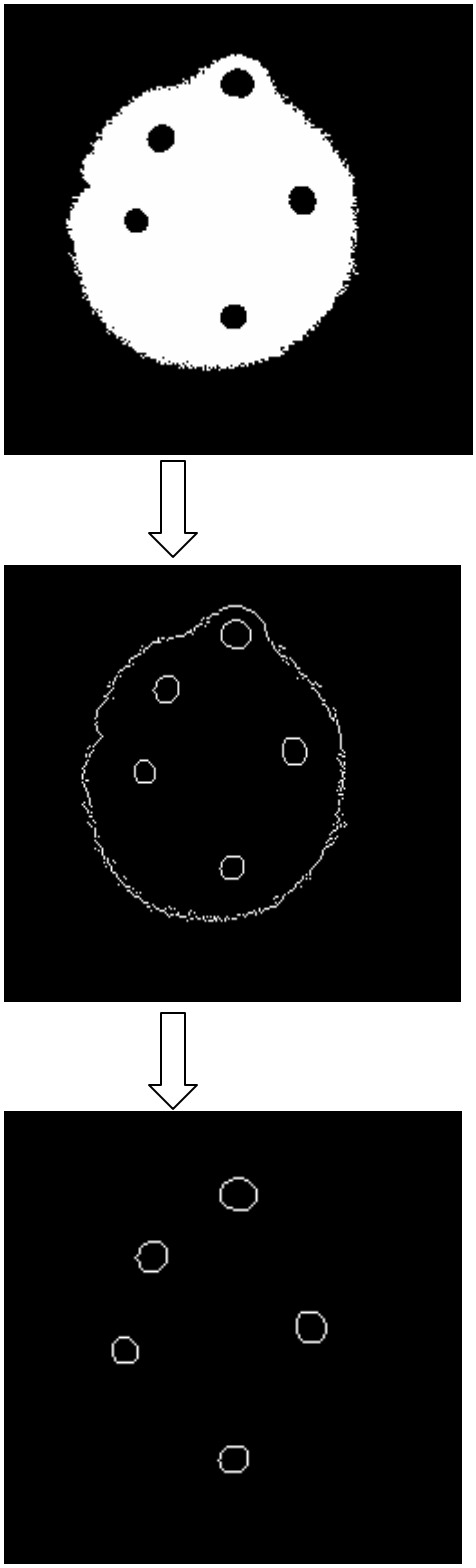

Step 3.Elimination of noises by basic cleaning up of image

Step 4. Edge Detection by Canny method

Step 5. Final image after image subtraction

Fig. D.2 Algorithm followed to arrive at final image for radius estimation

Now for each of these features obtained in the final image, any circle-fitting algorithm may be applied to fit a best circle. The radius of this best fitting circle approximately gives the radius of the seed defect.

It can be noticed that in the above procedure to determine radius of seed defect, a lot of image processing is involved. This consumes more time in real world complex situations. Hence an alternate approach is used in estimating the radius of the seed. This utilizes area of the seed as a whole to estimate the radius of the seed as compared to edge detection. The proposed approach is presented in the section 5.7.

APPENDIX E

RADIUS ESTIMATION & ZERO DEGREE REAL WORLD CONVERSION

E.1 Radius estimation using area

The following algorithm is followed to estimate the radius of the seed from the area of the feature:

1) The input image captured at 0˚ is read by the program

2) Processing of input image involves thresholding, suppression of light structures connected to image border, filling and cleaning

3) The area of the features in the image is then estimated using the statistical tool

4) This area is converted to real time area applying equation 5.6

5) The real time area is then equated to circular area to estimate the radius of the seed

The evolution of the final image is given in the steps below:

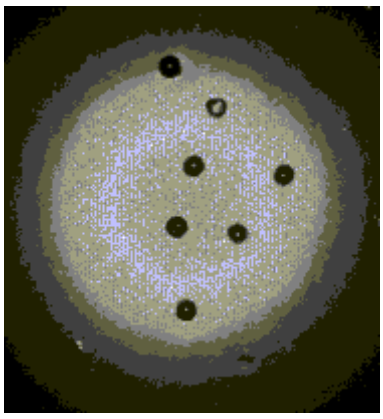

Step 1. Original Image captured by camera at 0˚ angle using self-illumination

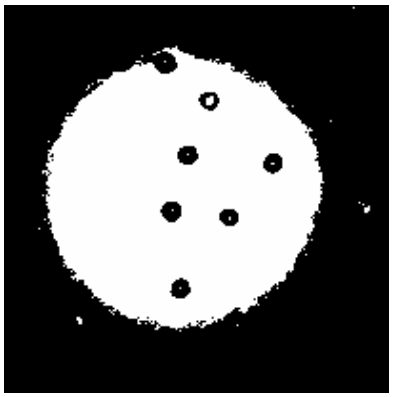

Step 2.Thresholded image at threshold intensity of 100

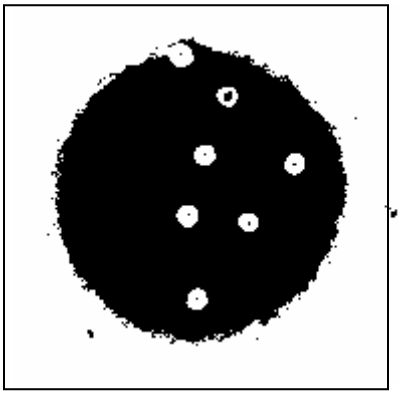

Step 3. Complement of the image obtained in step 2

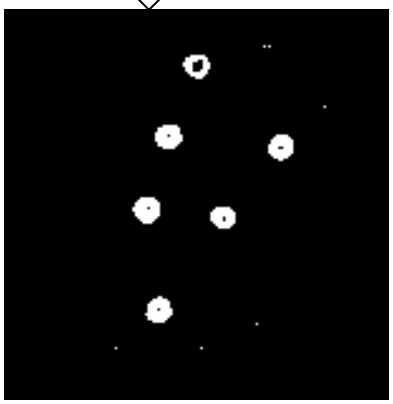

Step 4. Image obtained after suppression of light structures connected to image features

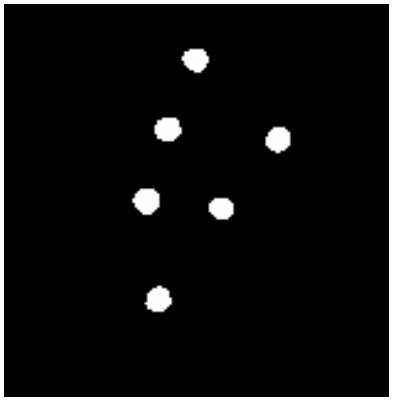

Step 5. Image after basic cleaning up and noise elimination

Fig. E.1 Evolution of Final Image using Image processing tool box in MATLAB

The image obtained in step 5 is then treated statistically to obtain the areas of features. This is then equated to circular area to obtain the radius of the seed utilizing eqn. 5.6.

E.2 Approximation in pixel co-ordinate conversion at 0˚

Tsai's work on calibration calls for the image to be placed at an angle to the camera (or vice versa) for accurate results with minimal normalized error. In order to estimate the size of the defect (radius), the image of the tile is captured at 0˚. Hence the proposed method by Tsai becomes invalid to use for converting pixel co-ordinates to real world co-ordinates. However, the image of the defect obtained in camera co-ordinate has to be translated to real time co-ordinate so as to know the size of the defect in real time. In order to do this, study was conducted on the image with an array of squares, the same as the one used for studying area variation across the plane of the tile. (Fig. E.2a) to know the maximum possible variation in position of features in the image obtained.

The real time origin is randomly fixed as (18.8,18.8) which is the centroid of the first square in the lower left corner (square 4 in Fig. E.2b) of the image. The real time distances between the centroids of the squares are known and so are the co-ordinates. Now image of this tile is captured at 0˚. The image is thresholded and the centroids of the squares are estimated using MATLAB. This gives the camera co-ordinates of the centroids of squares.

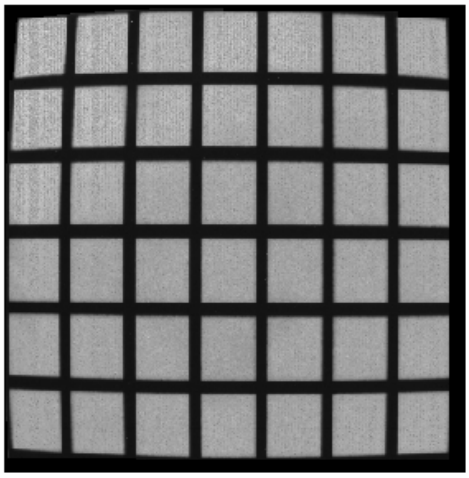

6	13	19	25	29	32	38
5	12	18	23	30	34	39
1	8	14	24	31	35	42
2	9	15	20	26	36	43
3	10	16	21	27	37	41
4	11	17	22	28	33	40

Fig. E.2a. Indicating the sample tile at 0° *Fig. E.2b. Indicating the square nos.*

From Fig E.2a, it is evident that there is distortion in the image at the ends. The distortion is more in the cells that are in the boundary than the cells that are in the center. As such, the following graphs (Fig. E.3a – E.3g) are plotted for the camera co-ordinates XC and YC against real world co-ordinates WXC and WYC. These graphs were plotted taking real time values of *"X" (WXC)* along X-axis and the corresponding *XC* and *YC* along Y-axis. The Y-co-ordinate in real time is constant for each of these graphs as the values are taken along rows (constant *WYC*).

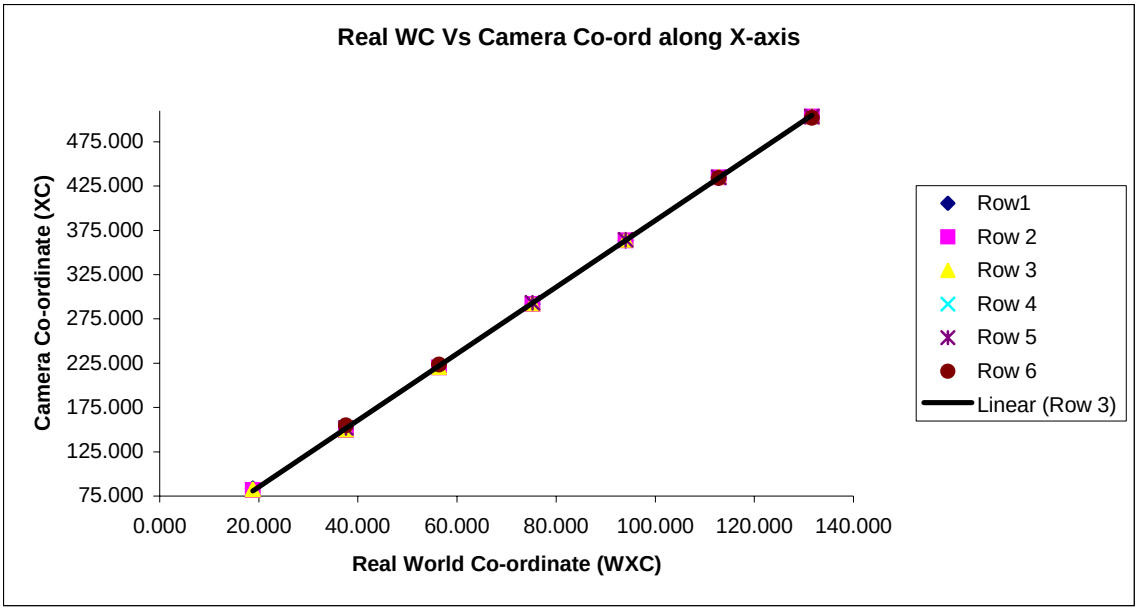

Fig. E.3a Variation of real world X co-ordinate and Camera co-ordinate along rows

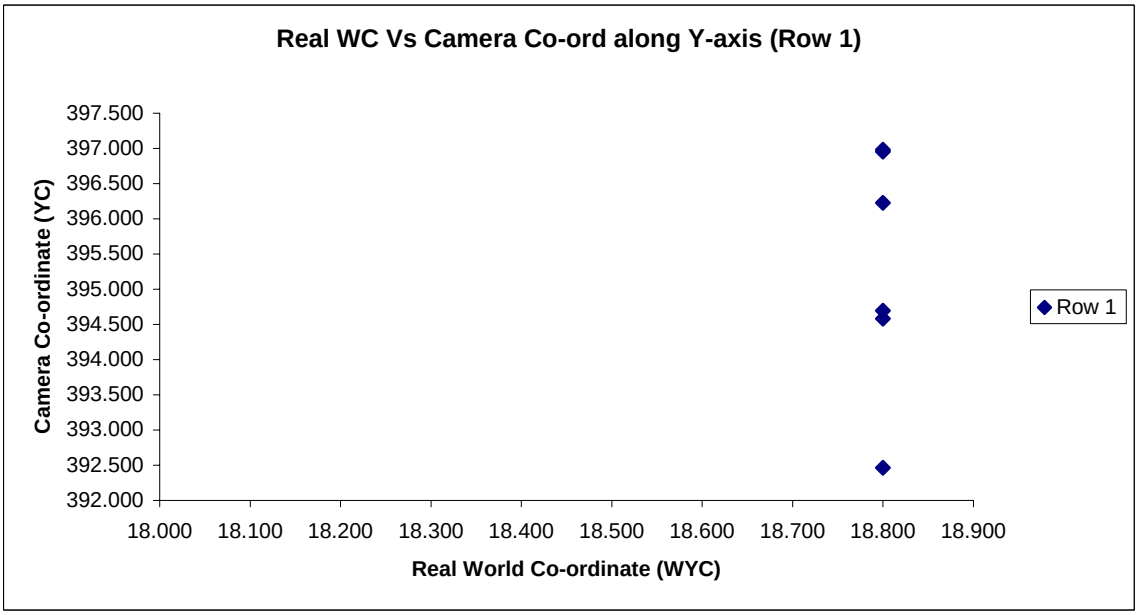

Fig. E.3b Variation of real world Y co-ordinate and Camera co-ordinate along Column 1

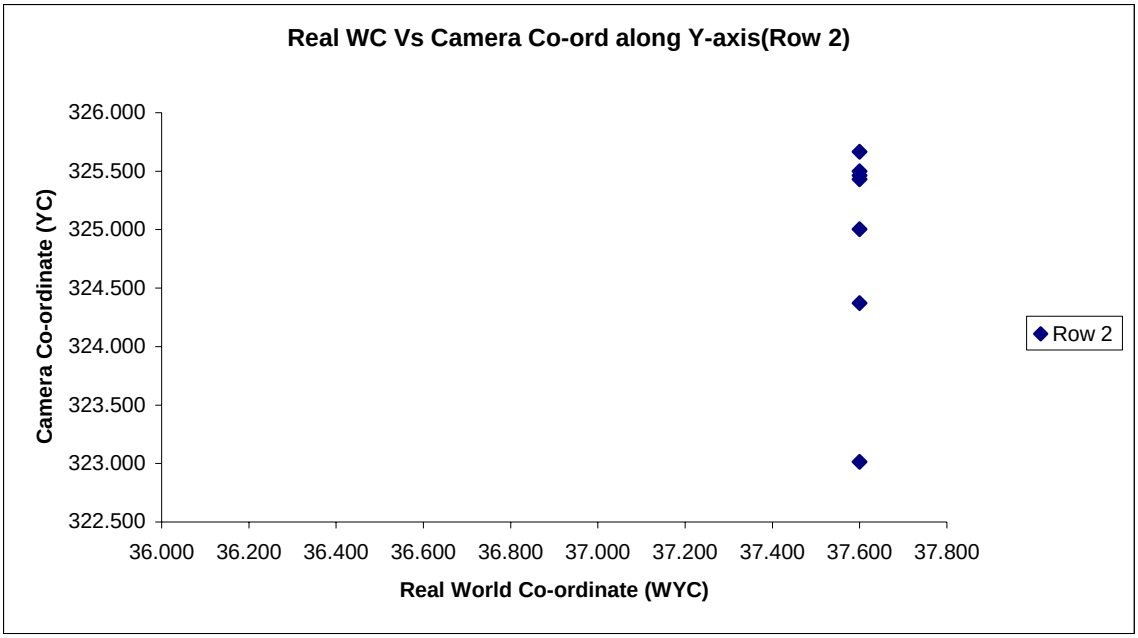

Fig. E.3c Variation of real world Y co-ordinate and Camera co-ordinate along Column 2

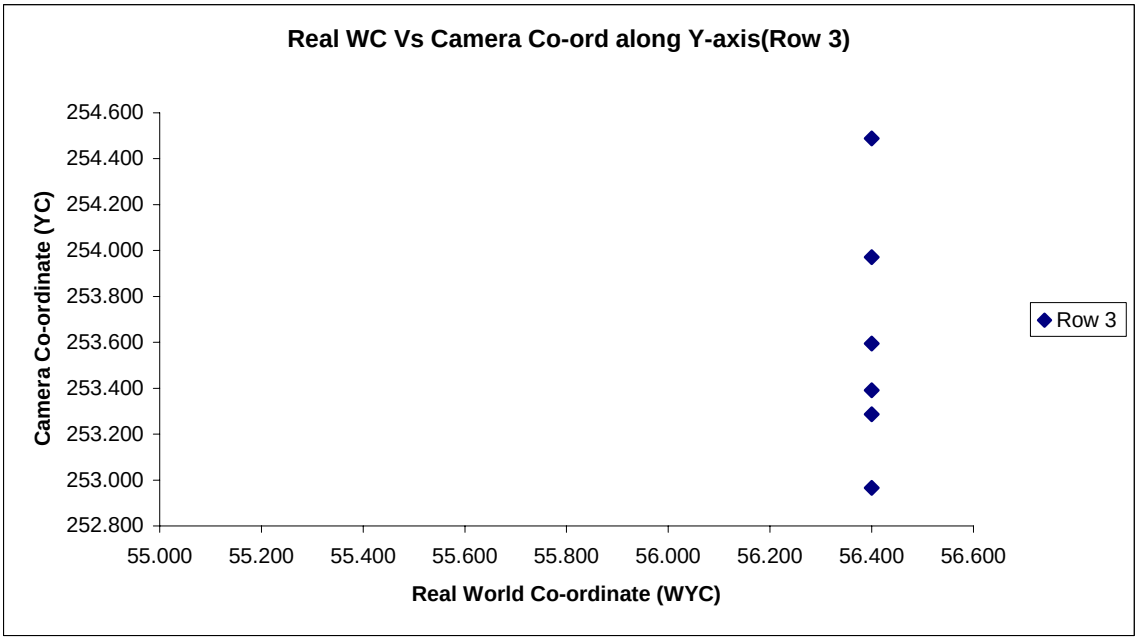

Fig. E.3d Variation of real world Y co-ordinate and Camera co-ordinate along Column 3

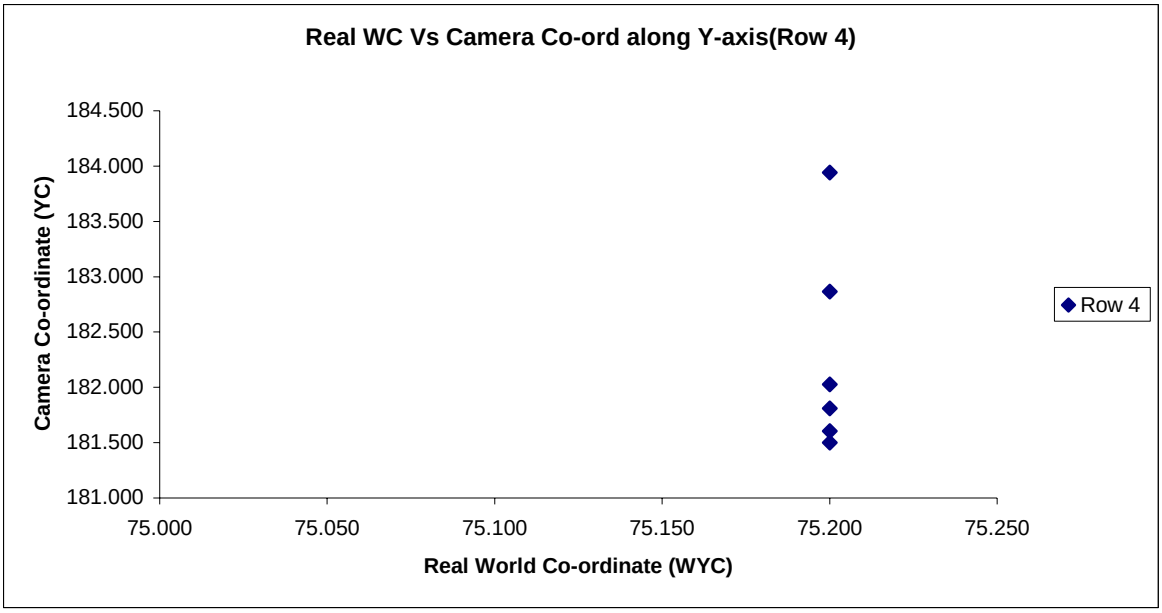

Fig. E.3e Variation of real world Y co-ordinate and Camera co-ordinate along Column 4

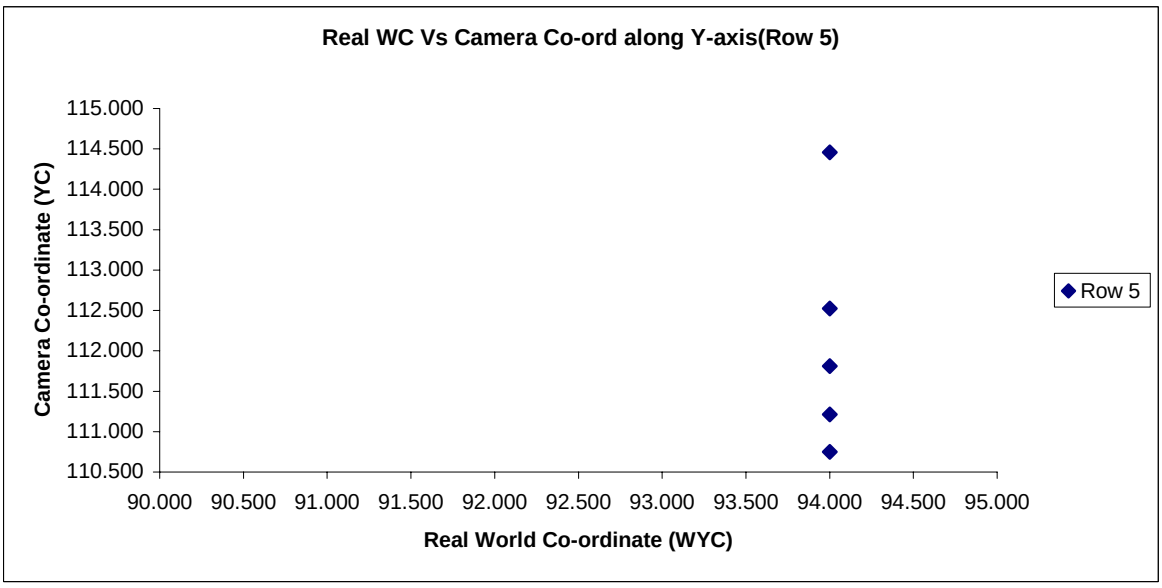

Fig. E.3f Variation of real world Y co-ordinate and Camera co-ordinate along Column 5

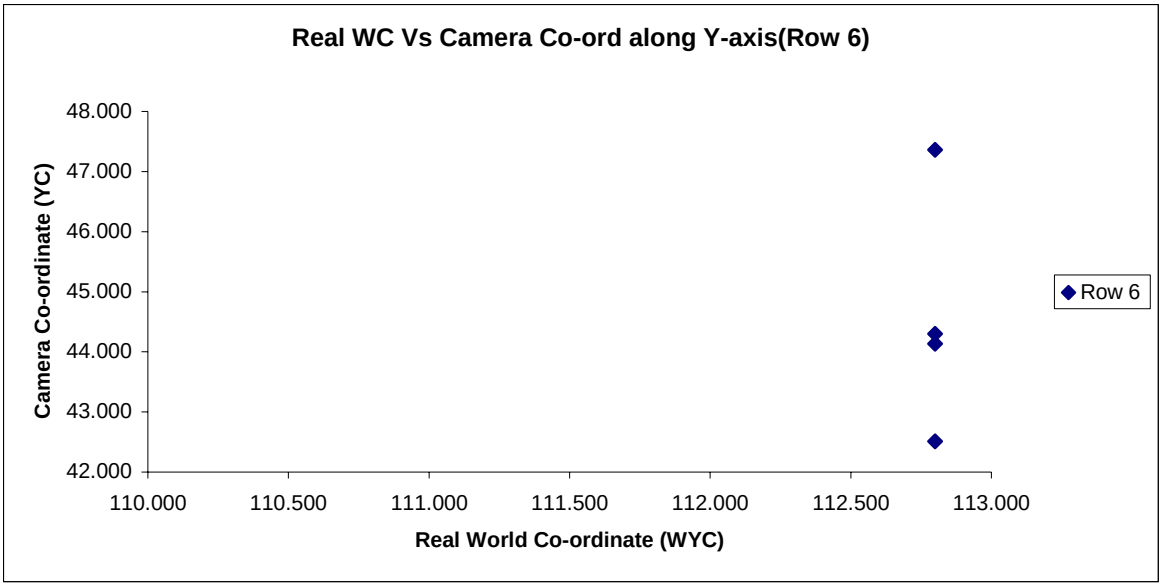

Fig. E.3g Variation of real world Y co-ordinate and Camera co-ordinate along Column 6

From the graphs presented above, it becomes evident that at all levels of rows a near linear relationship exists between the real world co-ordinates and the camera co-ordinates at 0˚ view angle. The range of pixel variation is in order of 3-5 pixels maximum in the extreme end rows and 1-3 pixels in the central rows. This variation seems nominal because of the fact that area is the main criteria in conducting the experiment for radius estimation and not the location. Hence a linear relationship may be assumed to exist among these variables. Hence transformation of camera co-ordinate to real world co-ordinate reduces to a point interpolation problem except that the area of interpolation has to be reached first in order to interpolate.

For e.g. for a given point in the camera plane *(xc, yc)*, the value of *xc* is constant along its axis parallel to Y-axis. Hence it is very necessary to interpolate in the area where the value of Y-axis is approximately *yc* so as to obtain better results. The same

holds good for *yc* also where the value of *yc* is interpolated in the area of approximate *xc*.

The interpolation program works the following way:

1) The known real world co-ordinates and the corresponding camera co-ordinates are inputted before hand from the image (fig. E.2).

2) The inputs are the camera co-ordinates *xc* & *yc*.

3) The closest column along which the *xc* lies is determined.

4) Now the value of *yc* is used to estimate the closest row in which the current camera co-ordinate lies.

5) Once the entire space data is reduced to a single block linear interpolation can be carried out in the region for both *xc* and *yc* to find the corresponding real world co-ordinates.

Once the camera co-ordinate can be interpolated to its approximate real world co-ordinate, the size of the pixel or the real world area enclosed by the single pixel (A_p) can be found. This was found to be 0.27mmx0.27mm. The radius of the seed can then be estimated using eqn. 5.6.

REFERENCES

1. Wong, A., Kamel, M., King, J., "Apparatus and method for inspection of surface quality of smooth surfaces", US patent no. 5090804, February, 1992.

2. Horigome, H., Tanabe, H., Nishifuji, K., "Method and Apparatus for performing Ultrasonic flaw detection", CA patent no. 2055285, November, 1991.

3. Smith, et al., "High speed flaw detecting system for reflective material", US patent no. 6097482, June 8, 1999.

4. Lee, F.H., "Two-mode surface defect testing system", US patent no. 5831725, October 16, 1996.

5. Pryor, T. R., Reynolds, R., Clarke, D., "Panel surface flaw inspection", CA patent no. 1273224, August 28, 1990.

6. Kammel, S., Leon, F.P., "Head-mounted display for interactive inspection of painted free form surfaces", Technologies and Applications. Proceedings of SPIE Vol. 5079, 2003.

7. Gnanaprakasam, P., "Characterization of seed defects in highly specular smooth coated surfaces", Masters thesis, 2004, University of Kentucky.

8. Nayar, S.K., Ikeuchi, K, “Surface reflection: Physical and Geometrical perspectives”, IEEE Transactions on Pattern Analysis and Machine Intelligence, Vol. 13, 1991.

9. Lawrence, B.W., Nayar, S.K., Oren, M., “Improved diffuse reflection models for Computer Vision”, International Journal of Computer vision, Vol. 30, 1998.

10. Horn, B., “Robot vision”, Cambridge, Mass.: MIT Press, 1998.

11. Parker, J. M and Lee, K.M., “Physically accurate Synthetic images for Machine Vision system design”, ASME Transaction Journal of Engineering for Industry, Vol. 121, 1999.

12. Parker, J. M., Gnanaprakasam, P., Ganapathiraman, S., Hou, Z., “Efficient 3-D characterization of surface defects in specular coatings”, Submitted for IEEE/ASME International conference, 2005.

13. Gnanaprakasam, P., Parker, J., Ganapathiraman, S. and Hou, Z., “Efficient 3-D Characterization of Raised Topological Defects in smooth Specular Coatings,” Computers in Industry, invited submission to Special Issue on Machine Vision, 2005

14. Parker, J. M., “An analytical and experimental investigation of physically accurate synthetic images for Machine vision design”, Doctoral thesis, 1996, Georgia Institute of Technology.

15. Tsai, R. Y., “A versatile camera calibration technique for high-accuracy 3D machine vision metrology using off- the- shelf TV cameras and lenses”, IEEE Journal of robotics and automation, Vol. RA-3, 1987.

16. Parker, J. M., Hou, Z., “A numerical investigation of diffuse images for effective defect detection”, Proceeding of the IMECH E Part B, Journal of Engineering Manufacturing, 2002.

17. Parker, J. M. and Lee, K. M., “Physically Accurate Synthetic Images for Machine Vision System Design”, ASME Trans. Journal of Engineering for Industry, Vol. 121, No. 4, pp. 763-770, 2002.

18. Parker, J. M. and Lee, K. M., “Image Synthesis Methodology for Algorithm Testing and Vision System Design”, Proceedings of the Institution of Mechanical Engineers Part B: Journal of Engineering Manufacture, Vol. 216, No. 5, 669-682, 2001.

19. Orchard, S., “Reflection and transmission of light by diffusing suspensions”, Journal of Optical Society of America, 59(12): 1584-1597, 1969.

20. Kuga, Y. and Ishimaru, A., “Retroreflectance from a dense distribution of spherical particles”, Journal of the Optical Society of America A, 1(8): 831-835, 1984.

21. Wolff, L.B., “A diffuse reflectance model for dielectric surfaces”, Proceedings of the SPIE conference on Optics, Illumination and Image Sensing for Machine Vision VII, Boston, MA, vol. 1822, pp. 60-73, 1992.

22. Bahar, E., “Review of full wave solutions for rough surface scattering and depolarization”, Journal of Geophysical Research, 92(C5): 5209-5224, 1987.

23. Tsang, L. and Ishimaru, A., “Backscattering enhancement of random discrete scatterers”, Journal of the Optical Society of America, A, 1(8): 836-839, 1984.

24. Torrance, K. and Sparrow, E., “Theory for off-specular reflection from roughened surfaces”, Journal of the Optical Society of America, 57: 1105-1114, 1967.

25. Sakai, I. and Sawabe, M., “A method for Surface Roughness Measurement by means of Light Reflectance”, Bulletin of Japan Society of Precision Engineering, 16(2), pp 123-124, 1982.

26. Lee, K.M., “Design concept of an Integrated Vision system for Cost-effective part presentation”, Transaction of the ASME Journal of Engineering for Industry, vol. 116, pp. 421-428, 1994.

27. Nixon, M. and Aguado, A., “Feature extraction and Image processing”, Replika press, 2002.

28. Parker, J. R., “Algorithms for Image processing and computer vision”, John Wiley & Sons, 1997.

29. Dupont Manual provided by Toyota Motor Manufacturing, Kentucky.

30. Lai, T., “A machine vision system design for the automated inspection of the appearance of specular painted surfaces”, Masters thesis, 1999, University of Kentucky

VITA

Subburengan Ganapathiraman was born on 26th August 1977 in Dindigul, India. He received his Bachelor of Technology degree in Mechanical Engineering from Pondicherry Engineering College, India in year 1998. He worked with Tractors and Farm Equipment Ltd., Chennai, India until 2001. In pursuit of his higher studies he attended the College of Engineering at University of Kentucky, Lexington. He is currently employed at Wafertech LLC, WA.